Double-differential-cross-section measurements of neutron scattering on ^{56}Fe

G. Gkatis,[1,2,3,*] M. Diakaki,[2] G. Noguere,[1] A. Oprea,[3] C. Paradela,[3] E. Pirovano,[4] and A. J. M. Plompen[3]

[1]*CEA/DES/IRESNE/DER/SPRC/LEPh, Cadarache, F-13108 Saint Paul Lez Durance, France*

[2]*Department of Physics, National Technical University of Athens, GR-15780 Athens, Greece*

[3]*European Commission, Joint Research Centre, B-2440 Geel, Belgium*

[4]*Physikalisch-Technische Bundesanstalt, D-38116 Braunschweig, Germany*

(Received 19 May 2025; accepted 7 July 2025; published 6 October 2025)

Measurements of neutron elastic and inelastic scattering on ^{56}Fe were performed at the Geel Electron Linear Accelerator (GELINA) of the EC-JRC. A highly enriched ^{56}Fe scattering sample was used to minimize the contribution of minor iron isotopes, ensuring the extraction of precise scattering cross-section data. The time-of-flight technique was utilized to determine the neutron incident energies, with scattered neutrons detected using the ELastic and Inelastic Scattering Array (ELISA), consisting of 32 liquid organic scintillators capable of neutron-photon discrimination via pulse-shape analysis, while a ^{235}U fission chamber was used to monitor the neutron fluence. The detectors are arranged into four arms, each comprising eight detectors at fixed angular positions relative to the neutron beam direction, facilitating the computation of both the angular distributions and the integral cross sections with the Gauss-Legendre quadrature. For elastic scattering, angular distributions, integral cross sections, and Legendre coefficients were determined across the energy range of 1 to 8 MeV. In the case of inelastic scattering, partial differential and angle-integrated cross sections from the first and the second excited states of ^{56}Fe were extracted in the energy regions from 2 to 5 MeV and from 3 to 6 MeV, respectively. Additionally, the total cross section was estimated in the energy interval from 2 to 2.5 MeV. The results of this work were compared with available experimental data, the most recent evaluated nuclear data libraries, and theoretical calculations performed using the TALYS 1.9 code.

DOI: 10.1103/b5n2-9kxn

I. INTRODUCTION

Iron is used in various applications within the nuclear industry, primarily due to its favorable mechanical and thermal properties. As a structural material, iron and its alloys are widely employed in the construction of nuclear reactors and other nuclear facilities. Due to their strength, corrosion resistance, and ability to maintain structural integrity even at high temperatures, iron-based materials are suitable for the construction of pressure vessels, structural supports for the reactor core, steam generators, piping systems, and other components inside a nuclear power plant [1–3]. This means that the steel alloy components are exposed to intense neutron flux during reactor operation. Additionally, these materials are used in the design of casks and containers for the storage and transportation of spent nuclear fuel [4]. These containers provide structural integrity and radiation shielding to ensure the safe handling and storage of radioactive materials. For these reasons, and to support the accurate modeling of neutron interactions within reactors and shielding systems, precise neutron cross-section data for iron are essential for reliable neutron transport simulations, reactor performance optimization, and the development of advanced nuclear systems.

Elemental iron consists of four naturally occurring stable isotopes, with ^{56}Fe being the most prevalent, comprising 91.75% of natural iron [5]. Even though iron is a common structural material in nuclear technology applications, its neutron-induced reaction cross sections remain very difficult to evaluate. Despite their importance, evaluations of iron available from various nuclear data libraries exhibit limitations in certain energy ranges and reaction channels relevant to advanced reactor applications. Uncertainty and sensitivity analyses have demonstrated that inaccuracies in neutron cross-section data for iron can significantly influence key integral parameters critical to the design and operation of advanced reactor systems [6,7]. As an example, as highlighted in Ref. [8], the ^{56}Fe elastic scattering cross section has been shown to significantly contribute to the uncertainty in key reactor parameters for the Versatile Test Reactor (VTR), a proposed 300 MWth sodium-cooled fast reactor [9]. It is stated that a relative uncertainty of 5–10% in the elastic scattering cross section of ^{56}Fe influences critical parameters such as the core multiplication factor and various reactivity feedback coefficients, which are essential for reactor design and performance assessment.

*Contact author: georgios.gkatis@ec.europa.eu

TABLE I. Elastic scattering data of ^{56}Fe available in the EXFOR library [17]. The name of the first author, the year of publication, the neutron energy range under study, the quantity (CS, cross section; DA, Differential cross section with respect to angle), and the number of points are listed.

Ref.		E_n range (MeV)	Quantity (Points)	
Rodgers (1967)	[18]	2.33	CS(1)	DA(5)
Kinney (1968)	[19]	4.60–7.57	CS(7)	DA(85)
Boschung (1971)	[20]	5.05–5.58	CS(2)	DA(19)
Morozov (1972)	[21]	1.80		DA(17)
Korzh (1977)	[22]	1.50–3.00	CS(4)	
Schweitzer (1978)	[23]	1.50–3.00	CS(1)	DA(12)
El-Kadi (1982)	[24]	7.96–13.90	CS(4)	DA(104)
Ramirez (2017)	[25]	0.80–7.96	CS(20)	DA(192)

To tackle these issues, ^{56}Fe was one of the six isotopes studied in the Collaborative International Evaluated Library Organization (CIELO) project [10], whose results were incorporated into the ENDF/B-VIII.0 [11] evaluation. A key concern identified was the lack of experimental angular distributions for elastic scattering on iron below 4 MeV, an energy region where theoretical models such as *R*-Matrix and Hauser-Feshbach become unreliable due to the complex structure of overlapping resonances observed in medium-mass nuclei [12–14]. These data are critical for reactor criticality and shielding calculations. Currently, the nuclear data for iron are under study by the International Nuclear Data Evaluation Network (INDEN) [15], as a continuation of the CIELO project, with the most recent results incorporated into the ENDF/B-VIII.1 evaluation [16] released in 2024. Despite progress made, further refinement requires high-resolution measurements in this energy region, where theoretical modeling alone is insufficient to constrain nuclear data for iron.

Although natural iron has been extensively measured, experimental data for individual isotopes, including ^{56}Fe, remain limited in the fast neutron energy region. For the elastic scattering on ^{56}Fe (see Table I), there are more measurements available for the differential cross section with respect to angle (DA) than for the elastic scattering cross section (CS), but these data are still sparse. All of the available experimental data for both DA and CS were obtained by using quasimonoenergetic neutron beams. While some datasets for the elastic scattering cross section in the range 1–8 MeV exist, they are limited and exhibit uncertainties reaching up to 20%. For the inelastic scattering on ^{56}Fe, several experimental datasets are available in EXFOR, based on neutron or γ-ray spectroscopy. In Tables II and III the available partial cross sections (CSP) and differential cross sections (DAP) for the first ($E_x = 0.8468$ MeV) and the second ($E_x = 2.0851$ MeV) excited states of ^{56}Fe are presented. However, only a limited number of experiments provide inelastic cross sections for neutron energies above 4 MeV, most of which rely on neutron spectroscopy. This is due to the challenges associated with γ-ray spectroscopy, particularly the complex level scheme of ^{56}Fe at higher energies, which complicates the identification of levels feeding the first and second excited states.

TABLE II. Partial inelastic scattering cross sections from the first excited level of ^{56}Fe (0.8468 MeV), available in EXFOR [17]. The name of the first author, the year of publication, the neutron energy range under study, the quantity (CSP, Partial cross section; DAP, Partial differential cross section with respect to angle), and the number of points are listed.

Ref.		E_n range (MeV)	Quantity (Points)	
Stelson (1952)	[26]	1.87		DAP(1)
Weddell (1956)	[27]	6.5		DAP(1)
Cranberg (1956)	[28]	2.25–2.45		DAP(26)
Kardashev (1962)	[29]	1.00–3.95	CSP(12)	
Bredin (1964)	[30]	1.95		DAP(10)
Gilboy (1965)	[31]	2.01–3.99	CSP(4)	
Tucker (1965)	[32]	0.864–1.10	CSP(31)	
Smith (1966)	[33]	1.13–1.50	CSP(26)	
Rodgers (1967)	[18]	2.33	CSP(1)	DAP(5)
Degtjarev (1967)	[34]	1.37–3.76	CSP(7)	
Kinney (1968)	[19]	4.60–7.55	CSP(7)	DAP(85)
Barrows (1968)	[35]	2.90	CSP(1)	
Tsukada (1969)	[36]	1.37–3.26		DAP(73)
Rogers (1971)	[37]	0.92–1.79	CSP(10)	
Boschung (1971)	[20]	5.05–5.58	CSP(2)	DAP(19)
Tomita (1973)	[38]	1.43–2.15		DAP(225)
Elbakr (1973)	[39]	0.891–1.74	CSP(8)	
Konobeevskii (1974)	[40]	0.862–1.18	CSP(67)	
Korzh (1975)	[41]	1.50–3.00	CSP(4)	
Almen-Ramström (1975)	[42]	2.02–4.50	CSP(11)	
Mittler (1975)	[43]	0.878–3.96	CSP(36)	
Korzh (1977)	[22]	1.50–3.00	CSP(4)	DAP (34)
Lebedev (1977)	[44]	4.70		DAP (3)
Schweitzer (1978)	[23]	3.40	CSP(1)	DAP (12)
Salama (1981)	[45]	2.02–3.96	CSP(6)	DAP (100)
Nemilov (1982)	[46]	0.893–5.00	CSP(32)	
El-Kadi (1982)	[24]	7.96–13.90	CSP(4)	DAP(89)
Negret (2013)	[47]	0.861–4.50	CSP(645)	
Beyer (2014)	[48]	0.847–9.56	CSP(30)	
Ramirez (2017)	[25]	1.50–7.96	CSP(14)	DAP (180)
Vanhoy (2018)	[49]	1.50–4.70	CSP(17)	
Pirovano (2019)	[50]	1.99–6.01		DAP(1530)

Consequently, the γ-ray emission pathways, which are crucial for accurate data interpretation, are affected, making the inelastic scattering data above 4 MeV more uncertain. The status of inelastic scattering cross-section data on ^{56}Fe has led to its inclusion on the High Priority Request List (HPRL) of the OECD/NEA Data Bank [51]. The targeted uncertainty for Accelerator-Driven Minor Actinides Burners is 2%, while for European Fast Reactors, it is 7–9%.

Given the challenges mentioned above, acquiring new experimental data on scattering cross sections is essential for addressing discrepancies in the existing ones and reducing uncertainties in the evaluated nuclear data libraries of iron. The aim of this study is to provide, for the first time, high-resolution data of cross sections and neutron angular distributions for both elastic and inelastic scattering on ^{56}Fe in the fast neutron energy range. To achieve this, a highly enriched ^{56}Fe sample was used along with a white

TABLE III. Partial inelastic scattering cross sections from the second excited level of ^{56}Fe (2.0851 MeV), available in EXFOR [17]. The name of the first author, the year of publication, the neutron energy range under study, the quantity (CSP, Partial cross section; DAP, Partial differential cross section with respect to angle), and the number of points are listed.

Ref.		E_n range (MeV)	Quantity (Points)	
Weddell (1956)	[27]	6.5		DAP(1)
Kardashev (1962)	[29]	1.00–3.95	CSP(6)	
Gilboy (1965)	[31]	2.01–3.99	CSP(3)	
Tucker (1965)	[32]	0.864–1.10	CSP(23)	
Degtjarev (1967)	[34]	1.37–3.76	CSP(4)	
Kinney (1968)	[19]	4.60–7.55	CSP(12)	
Barrows (1968)	[35]	2.90	CSP(1)	
Tsukada (1969)	[36]	1.37–3.26		DAP(34)
Boschung (1971)	[20]	5.05–5.58	CSP(2)	DAP(19)
Korzh (1975)	[41]	1.50–3.00	CSP(1)	
Almen-Ramström (1975)	[42]	2.02–4.50	CSP(7)	
Mittler (1975)	[43]	0.878–3.96	CSP(21)	
Korzh (1977)	[22]	1.50–3.00	CSP(1)	DAP (9)
Nemilov (1982)	[46]	0.893–5.00	CSP(7)	
Negret (2013)	[47]	0.861–4.50	CSP(288)	
Beyer (2014)	[48]	0.847–9.56	CSP(14)	
Ramirez (2017)	[25]	1.50–7.96	CSP(6)	
Vanhoy (2018)	[49]	1.50–4.70	CSP(13)	

neutron source and the time-of-flight method, while the scattering events were detected using an array of liquid organic scintillators.

II. EXPERIMENTAL CONDITIONS

The experiments were conducted at the Geel Electron Linear Accelerator (GELINA) neutron time-of-flight facility, operated by the Joint Research Centre of the European Commission in Geel (EC-JRC Geel) [52,53]. GELINA provides pulsed white neutron beams using a linear electron accelerator. In this process, electrons are accelerated to high energies and directed in short bursts of approximately 2 ns onto a depleted uranium disk, which serves as the neutron-producing target. The interaction of the electrons with the target material generates photons through the bremsstrahlung process, followed by neutron production via photonuclear reactions, such as (γ, n) and (γ, f) in ^{238}U nuclei. The resulting neutrons exhibit a broad energy spectrum, extending from a few keV to nearly 20 MeV, and are emitted isotropically. The neutrons are collimated and guided along specific flight paths to the experimental setups positioned at designated measuring stations. For this study, the direct flux configuration was used, delivering an unmoderated neutron beam ideal for fast energy range measurements.

For this experiment, a highly enriched ^{56}Fe sample was used. The properties of the sample are summarized in Table IV. The measured areal density of the sample was 8.78×10^{-3} g/cm^2 with a 0.2% uncertainty. The scattering sample was positioned 27.037(5) m from the neutron-producing target, precisely at the spectrometer's sample location, at a 29.5(1)-cm distance from the detectors. The neutron beam diameter at the sample position was determined using a photographic film and measured to be 4.9(2) cm. Two sets of measurements were conducted: one with the sample in the neutron beam (sample in) for approximately 500 hours and another without the sample (sample out) lasting 350 hours. The purpose of the sample-out measurement was to evaluate the background contribution from neutrons scattering in the air and surrounding materials before reaching the detectors.

TABLE IV. Isotopic composition and geometrical characteristics of the enriched ^{56}Fe scattering sample used in the present work.

Fe isotope	^{54}Fe	^{56}Fe	^{57}Fe	^{58}Fe
Abundance (%)	0.16(1)	99.77(1)	0.07(1)	<0.01
Mass (g)		31.396(10)		
Diameter (mm)		70.068(1)		
Thickness (mm)		1.00(1)		
Molar mass (g/mol)		55.935(1)		
Areal Density (g/cm^2)		0.814(2)		
Areal Density (atoms/barn)		0.00878(1)		

III. THE ELISA SPECTROMETER

The ELastic and Inelastic Scattering Array (ELISA) was utilized to detect the scattered neutrons (Fig. 1). The spectrometer is one of the several experimental setups installed at the GELINA facility and is used for high-resolution measurements of neutron elastic and inelastic scattering cross sections and angular distributions in the fast neutron energy range. The setup is extensively detailed in Refs. [50,54–59]; here only a brief overview of the main components is provided.

The setup consists of two main components: 32 liquid organic scintillators for detecting scattered neutrons, and a ^{235}U fission chamber for measuring the neutron flux. The scintillators are arranged in four arms, each consisting of eight detectors, positioned at specific angles relative to the neutron

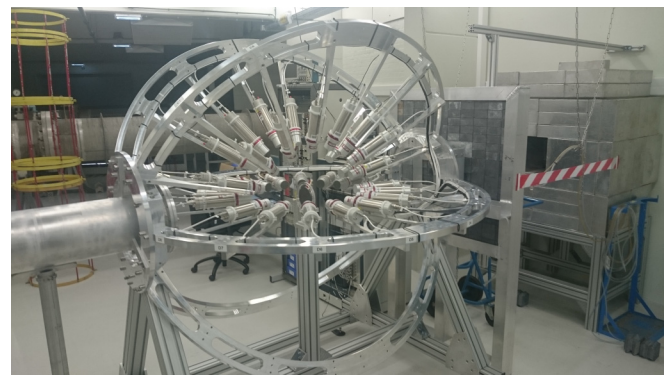

FIG. 1. Photograph of the ELISA spectrometer. The neutron beam enters from the right, passes through the fission chamber behind the lead wall, and then reaches the scattering sample. The lead wall functions as the final collimator.

TABLE V. Detection angles relative to the neutron beam direction, along with their calculated cosines and assigned weights. The uncertainties associated with the detection angles reflect the precision in the assembly of the detector support frame.

Angle (def)	163.8(1)	142.8(1)	121.7(1)	100.6(1)	79.4(1)	58.3(1)	37.2(1)	16.2(1)
Cosine	−0.9603(5)	−0.7967(11)	−0.5255(15)	−0.1834(17)	0.1834(17)	0.5255(15)	0.7967(11)	0.9603(5)
Weight	0.1012	0.2224	0.3137	0.3627	0.3627	0.3137	0.2224	0.1012

beam direction (Table V). The detection angles are meticulously selected so that their corresponding cosines align with the zeros of the Legendre polynomial of the eighth order, which enables the calculations of the integral cross section using the Gauss-Legendre quadrature rule:

$$\sigma_{\mathrm{el/inl}}(E) = 2\pi \sum_{i=1}^{8} w_i \frac{d\sigma_{\mathrm{el/inl}}}{d\Omega}(E, \theta_i), \tag{1}$$

where $\frac{d\sigma_{\mathrm{el/inl}}}{d\Omega}(E, \theta_i)$ is the differential elastic or inelastic neutron scattering cross section as a function of the detection angle θ_i, and w_i are the corresponding weighting factors.

The two arms of the ELISA spectrometer are equipped with detectors using the EJ301 scintillation material [60], in which neutron detection is based on *n-p* scattering, while the other two arms use the EJ315 scintillation material [61], which relies on *n-d* scattering for neutron detection. These scintillators have fast timing properties and can achieve a time resolution of under 1 ns, making them well suited for time-of-flight measurements. Additionally, they are highly effective for neutron spectrometry, as photons and neutrons can be distinguished through pulse-shape analysis. The choice of two different detector types, proton based (EJ301) and deuterium based (EJ315), is because of the different pulse height responses produced by each detector. In the case of EJ301, the pulse height response follows a flat distribution, due to the isotropic nature of *n-p* scattering in the center-of-mass frame. In contrast, for EJ315, *n-d* scattering is not isotropic, resulting in a dominant backscattering peak in the pulse height distribution. This difference between the two detector types serves as a cross-check and helps to identify potential systematic errors during data analysis.

The fission chamber contains eight UF_4 deposits on five aluminum foils (84 mm in diameter, 20 μm thick), produced at the JRC-Geel via evaporation. Each deposit is shaped by a 70-mm evaporation mask. The total areal density of ^{235}U across all deposits was measured at 4095(12) μg/cm^2 using α counting. Two single-sided foils are positioned at the front and back, while three double-sided foils are spaced 14 mm apart in the middle. Each deposit faces a 25-μm-thick aluminum anode, placed at a distance of 7 mm, for the collection of the charge deposited by the fission fragments. The chamber is filled with P10 gas at atmospheric pressure. The neutron fluence is determined by correlating the fission fragment counts with incident neutrons using the ^{235}U(n, f) standard reaction cross section as described in Ref. [59]. In Fig. 2, the neutron fluence that impinged on the ^{56}Fe scattering sample during the measurement is presented, as extracted following the analysis described in Ref. [57].

The scintillator data acquisition system (DAQ) is based on a digitizer system consisting of eight cards, each with four input channels. These digitizers (SP Devices, model ADQ14DC-4A-VG-PXIe) offer a 14-bit amplitude resolution and a 500 MS/s sampling rate. Synchronization is ensured via an external 10-MHz reference signal from a clock generator, and the acquired waveforms and time stamps are stored for offline analysis. For the fission chamber, data acquisition is handled using NIM electronics, which process the fission fragment signals before digitization.

IV. ANALYSIS

The data analysis method for the ELISA spectrometer is detailed in Refs. [54,57]. A brief overview of the key components of the analysis is presented below. The neutron differential elastic or inelastic scattering cross section was calculated using the following expression:

$$\frac{d\sigma_{\mathrm{el/inl}}}{d\Omega}(E, \theta) = \frac{N'_{\mathrm{el/inl}}(E, \theta)}{\Delta\Omega \rho_T \Phi(E) A_b}, \tag{2}$$

where E is the incident neutron energy, $N'_{\mathrm{el/inl}}$ represents the corrected count of elastic or inelastic scattering events, $\Delta\Omega$ is the detector's solid angle, ρ_T is the areal density of the sample in atoms/barn (Table IV), $\Phi(E)$ is the neutron fluence (Fig. 2), and A_b is the cross-sectional area of the neutron beam, which is accounted for in the calculation of the neutron fluence and thus cancels out. The angle θ will henceforth implicitly refer to the eight angles in the ELISA setup.

In the first stage of the data analysis, the digitized scintillator signals are processed. For each recorded waveform, the total charge and the corresponding time stamp are

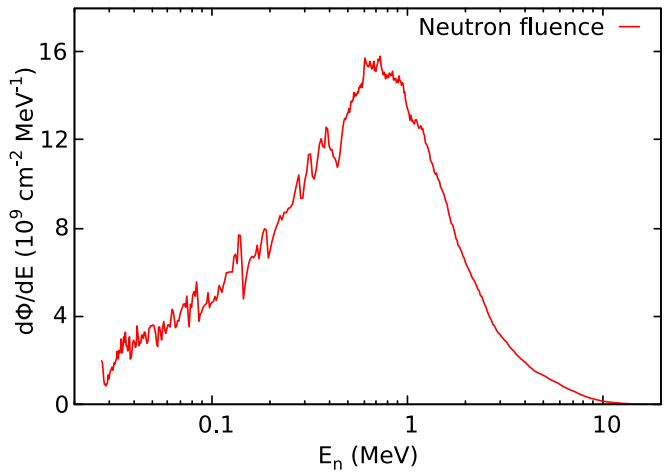

FIG. 2. The neutron fluence on the ^{56}Fe sample as a function of incident neutron energy, corresponding to a total measurement duration of 500 hours.

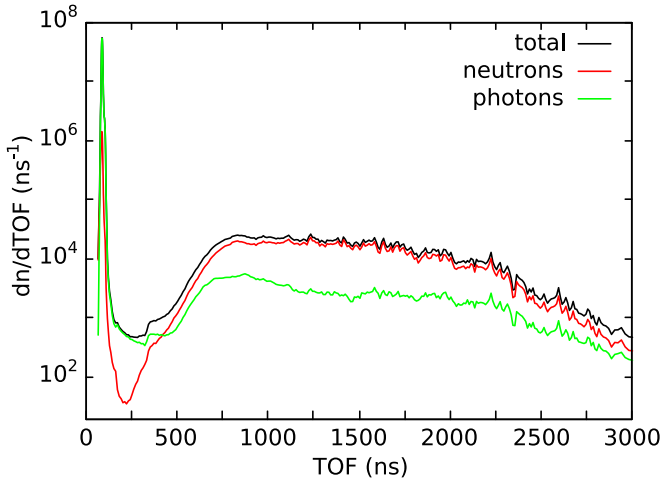

FIG. 3. The time-of-flight spectra from an EJ315 detector placed at the 16.2° detection angle. The graph shows the total recorded events (black line) alongside the neutron (red line) and photon (green line) events, which were distinguished using pulse-shape discrimination.

extracted. To improve time resolution, the time stamps are corrected using the constant fraction discrimination (CFD) algorithm [62–64]. The events recorded by the scintillators during the measurements consist of a combination of neutrons from elastic or inelastic scattering on the sample, and photons from bremsstrahlung scattering, or γ rays emitted via inelastic scattering or neutron capture on the sample and surrounding materials. To differentiate between neutron- and photon-induced events, the charge integration method was applied [65–67]. Signals were integrated over both short and long time intervals, and the pulse shape discrimination (PSD) factor was defined as the ratio of the integral of the pulse tail to the total integrated charge. In Fig. 3 an example of the resulting time-of-flight histogram after the pulse-shape discrimination for an EJ315 detector positioned at 16.2° is presented. It is observed that the time-of-flight spectrum exhibits a distinct peak at around 91 ns, which represents the arrival time of bremsstrahlung photons at the detectors (so-called γ flash). The FWHM of the γ-flash peak, serving as the lower limit for time resolution, was measured at 10 ns for the detectors in the ELISA setup during this experiment. At the given distance from the source, a time resolution of 10 ns corresponds to a 10-keV energy resolution at 1 MeV, 53 keV at 3 MeV, 113 keV at 5 MeV, and 189 keV at 7 MeV.

After signal processing, the next step is to characterize the detectors' response function $R(L, E)$, which represents the probability that a particle with energy E produces a light pulse of amplitude L. This study utilizes a combination of experimental measurements and Monte Carlo simulations, as described in Refs. [68–71]. Before each new experiment at the ELISA spectrometer, the detectors undergo a full characterization to ensure stability and identify any potential issues that may have arisen during the measurements.

Starting with the response to γ rays, the light output produced by electrons for the scintillators used at ELISA is described by the linear function

$$L(E_e) = A_1(E_e + A_0), \tag{3}$$

where A_1 is an arbitrarily chosen scaling parameter set to 1 in the present work, following the convention of measuring light in terms of equivalent electron energy deposition [72], and A_0 is an energy offset set to -5 keV, accounting for the quenching effects in the scintillators at small energies [73]. Calibration measurements were conducted at the start of and throughout the experiments using five γ-ray sources (^{137}Cs, ^{207}Bi, ^{22}Na, ^{232}Th, and AmBe) to monitor detector stability. Additionally, Monte Carlo simulations of these measurements were performed using the MCNP6.2 code [74,75]. The simulated light output distributions for each source were folded with the resolution function and then fitted to the corresponding experimental light output histograms. This fitting process allowed for the determination of the final resolution function parameters for each detector.

To accurately determine the neutron response, it is essential to account for the nonlinear light output behavior of charged particles heavier than electrons, in this case, protons (EJ301) and deuterons (EJ315). In this work, the empirical formula proposed by Kornilov *et al.* [70] was employed to describe the light output distributions:

$$L(E_r) = A_1 E_r + \frac{A_2 E_r^2}{E_r + A_3}, \tag{4}$$

where E_r represents the recoil energy of the charged particle, and A_1, A_2, and A_3 are detector-specific parameters that must be determined experimentally. To achieve this, a dedicated calibration experiment was conducted at the ELISA spectrometer using a natural carbon sample. Carbon was selected due to its high inelastic scattering threshold (4.81 MeV), ensuring that only elastically scattered neutrons reach the detectors below this energy. By selecting short time-of-flight intervals (10 ns) corresponding to narrow neutron energy ranges, the simulated light output distributions were systematically fitted to the experimental data at each energy. The extracted parameters from these individual fits were then combined to obtain a set of values best suited for the entire neutron energy range. This approach allowed for the development of a response function model individually for each detector, which was subsequently incorporated into the ^{56}Fe data analysis. An example of this implementation is shown in Fig. 4.

Once the neutron time-of-flight spectra were obtained for each detector, the next step involved subtracting the background contribution. Background events primarily originate from neutrons scattered on air and surrounding materials before reaching the detectors. To account for this, a reference measurement was performed without the sample, and the resulting background spectrum was scaled and subtracted from the sample-in data. The normalization factor was determined based on the fission fragment counts recorded in the ionization chamber. On average, background events constituted approximately 30–40% of the recorded signals in each detector. In Fig. 5, the experimental neutron background at the 163.8° detection angle is compared to the corresponding simulated one. The simulated background represents only beam neutrons that scattered on air and then reached the detector. This component

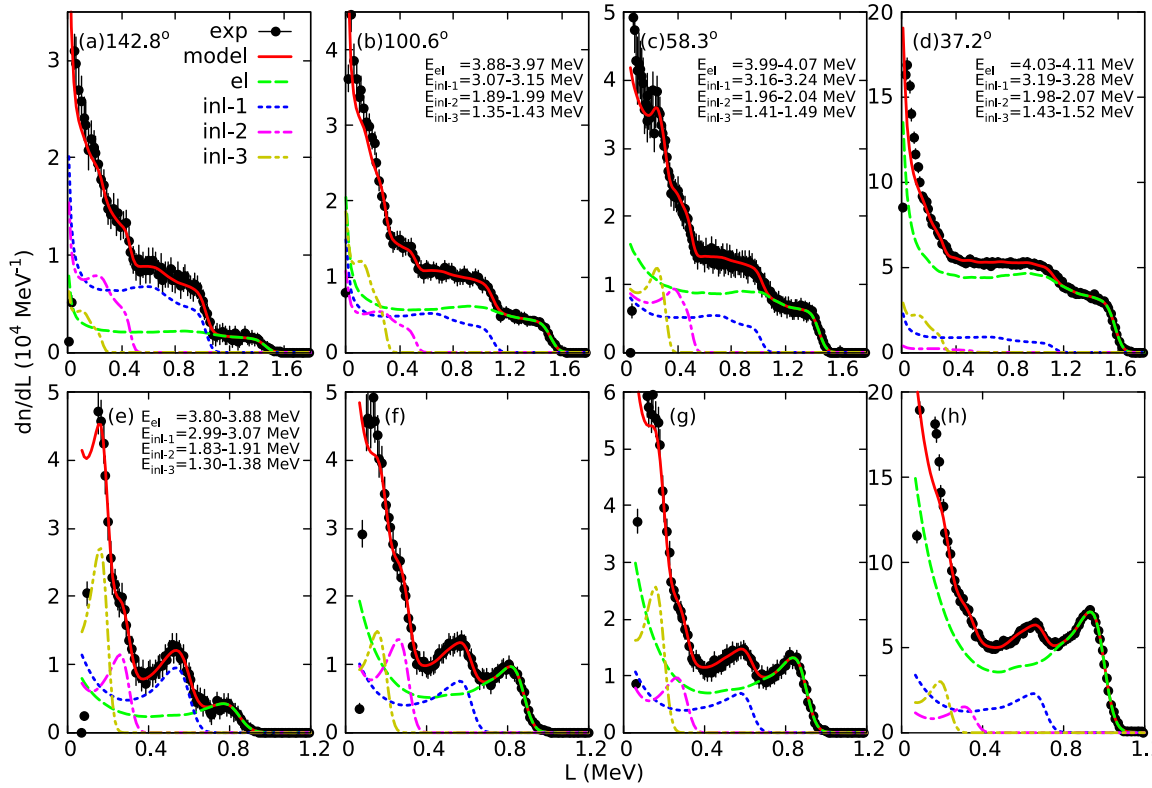

FIG. 4. Light output distributions for the time-of-flight interval from 976 to 986 ns. The graphs correspond to the same four different detection angles for both the [(a)–(d)] EJ301 (n,p) and [(e)–(h)] EJ315 (n,d) detectors. The experimental values (exp) are presented along with their associated response (model) and their different components from elastic scattering (el), and inelastic scattering from the first, second, and third excited states (inl-1, inl-2, inl-3). The corresponding neutron energies after an elastic ($E_{\rm el}$), and inelastic scattering from the first, second, and third levels ($E_{\rm inl\text{-}1}$, $E_{\rm inl\text{-}2}$, $E_{\rm inl\text{-}3}$) are also given in the graphs.

was extracted using the MCNP6.2 code and the PTRAC output option. It is observed that the two background spectra are in agreement within the uncertainty of the simulation, which validates the fact that the majority of the background events are generated from neutron scattering in the air.

Following the discrimination of photon-induced events and the subtraction of background contributions, the final step was to separate elastic and inelastic neutron scattering events. To achieve this, the time-of-flight spectrum was divided into 10-ns intervals, and the corresponding light output distributions were analyzed. Figure 4 illustrates examples of these distributions for both types of detectors positioned at four different angles. The selected time-of-flight window (976–986 ns) corresponds to an incident neutron energy range of 4.05–4.14 MeV. Through kinematic calculations, the energies of neutrons scattered elastically ($E_{\rm el}$) or inelastically ($E_{\rm inl}$) were determined for each time-of-flight (TOF) interval. These two types of events produce distinct but overlapping light output distributions (see Fig. 4). To isolate the elastic scattering component, a threshold was applied to exclude inelastic scattering contributions. This threshold was set at the maximum light output expected from an inelastic event, considering the detector's resolution broadening. The modeled detector response $R(L, E_{\rm el})$ for neutrons with energy $E_{\rm el}$ was scaled by a factor (λ) to match the experimental data above the threshold. The resulting function, $R_{\rm fit}(L, E_{\rm el}) = \lambda\, R(L, E_{\rm el})$ describes the contribution of elastic scattering events to the total light output distribution. The number of elastic scattering events was then determined using the expression

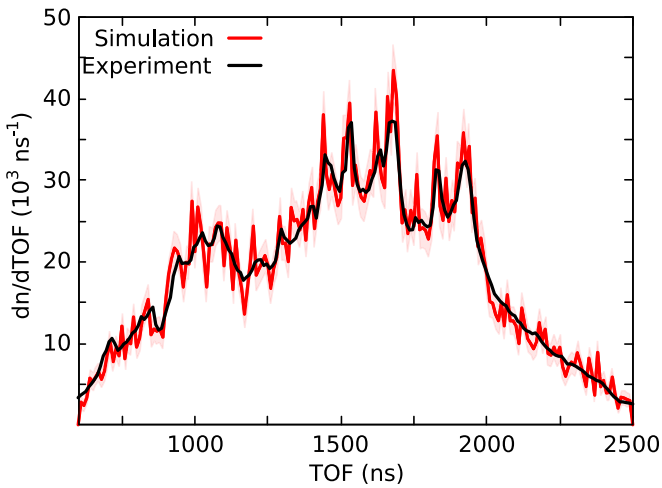

FIG. 5. Comparison between the experimental and the simulated neutron background at the 163.8° detection angle.

$$N_{\rm el}({\rm TOF},\theta) = \frac{1}{\epsilon(E_{\rm el})|L_{\rm thr}\,\Delta\Omega}\int_{L_{\rm thr}} R_{\rm fit}(L, E_{\rm el})dL, \quad (5)$$

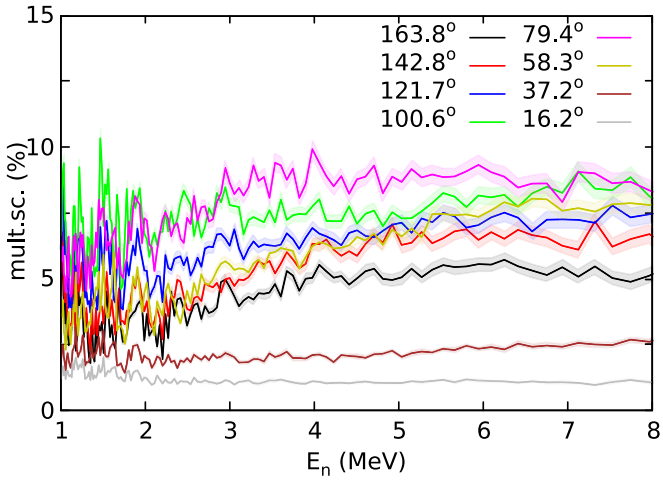

FIG. 6. Multiple scattering correction percentage as a function of the incident neutron energy across all eight detection angles.

where N_{el} represents the number of elastic scattering events per 10-ns time-of-flight interval and detection angle, $\Delta\Omega$ is the detector's solid angle, and $\epsilon(E_{\mathrm{el}})|_{L_{\mathrm{thr}}}$ denotes the detection efficiency at the threshold light output L_{thr}, calculated using $\epsilon(E_{\mathrm{el}})|L_{\mathrm{thr}} = \int_{L_{\mathrm{thr}}} R(L, E_{\mathrm{el}})\, dL$. The same approach was applied to extract inelastic scattering events corresponding to the first and the second excited states of ^{56}Fe. In this case, additional thresholds were introduced to remove events from the different excited states, while the elastic scattering contribution was subtracted accordingly.

The number of neutron-induced events corresponding to different scattering processes was corrected for multiple scattering effects before being used in the cross-section calculations. Multiple scattering occurs when beam neutrons interact more than once within the ^{56}Fe sample before reaching a detector. In this study, the correction factor (f_{msc}) for such events was determined through Monte Carlo simulations using the MCNP6.2 code. The simulation incorporated the complete spectrometer geometry and accurately modeled the neutron source properties based on the experimental conditions. The PTRAC feature of mcnpwas employed to track the history of each neutron detected, identifying events where neutrons underwent multiple interactions within the sample before recorded. The correction factor was then calculated as the ratio of these multiple scattering events to the total detected events, allowing for a time-of-flight-dependent correction for each detector (see Fig. 6). The corrected differential scattering yield was obtained using

$$N'_{\mathrm{el/inl}}(\mathrm{TOF}, \theta) = (1 - f_{\mathrm{msc}}) \cdot N_{\mathrm{el/inl}}(\mathrm{TOF}, \theta), \qquad (6)$$

where $N_{\mathrm{el/inl}}$ represents the uncorrected number of elastic or inelastic scattering events per 10-ns time-of-flight interval and detection angle, while $N'_{\mathrm{el/inl}}$ denotes the corrected values.

Once all individual components were determined, the differential cross sections were computed using Eq. (2), followed by the calculation of the angle-integrated cross sections via Eq. (1). Given that each scattering angle at the ELISA spectrometer was covered by four detectors, the final cross-section values for each angle were obtained by averaging the results from all four detectors, while ensuring that common uncertainty components were accounted for separately and not averaged. The total uncertainty associated with the calculated cross sections was determined through uncertainty propagation using the root-sum-square method. This involved summing the squares of the partial derivatives of each contributing parameter, weighted by their respective uncertainties, and taking the square root of the total sum. The statistical uncertainty was primarily influenced by the number of scattered neutrons detected and the fission fragment yield from the ^{235}U deposits. Additionally, systematic uncertainties arising throughout the data analysis process are summarized in Table VI.

TABLE VI. List of the systematic uncertainties associated with the ^{56}Fe data analysis.

Contribution	Uncertainty
Sample areal density	0.2%
Fission chamber efficiency	1%
^{235}U(n, f) cross section	1.1–1.2%
^{235}U deposits mass	0.3%
Multiple scattering correction	3–7%

To validate the analysis procedure, the neutron elastic scattering cross section of natural carbon was determined. Carbon serves as an excellent reference since its differential elastic scattering cross section is considered a standard below 1.8 MeV and the elastic scattering is well known up to 6.45 MeV with an uncertainty below 1% [76]. As previously stated, a specialized experiment was conducted at ELISA using a natural carbon sample to determine the parameters of the light output function [Eq. (4)] for the neutron response models.

The integrated elastic scattering cross section is shown in Fig. 7, along with the JEFF-3.3 [77] and ENDF/B-VIII.1 [16] evaluations. To account for the spectrometer's energy

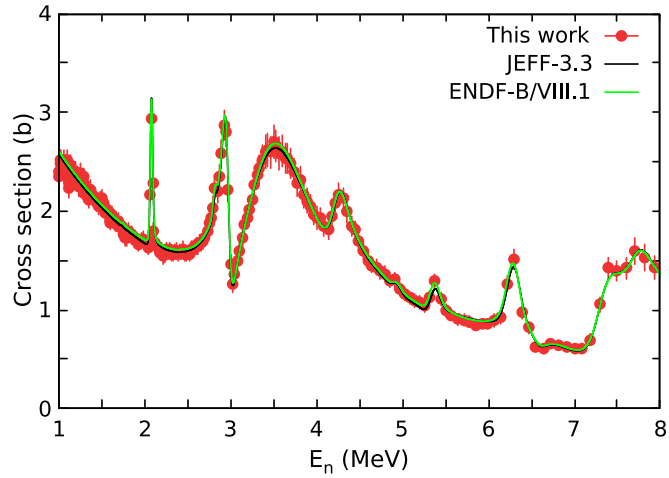

FIG. 7. Angle-integrated cross section of neutron elastic scattering on $^{\mathrm{nat}}$C as a function of the neutron incident energy compared to the JEFF-3.3 [77] and ENDF/B-VIII.1 [16] evaluations folded with the experimental energy resolution of the measurement [78].

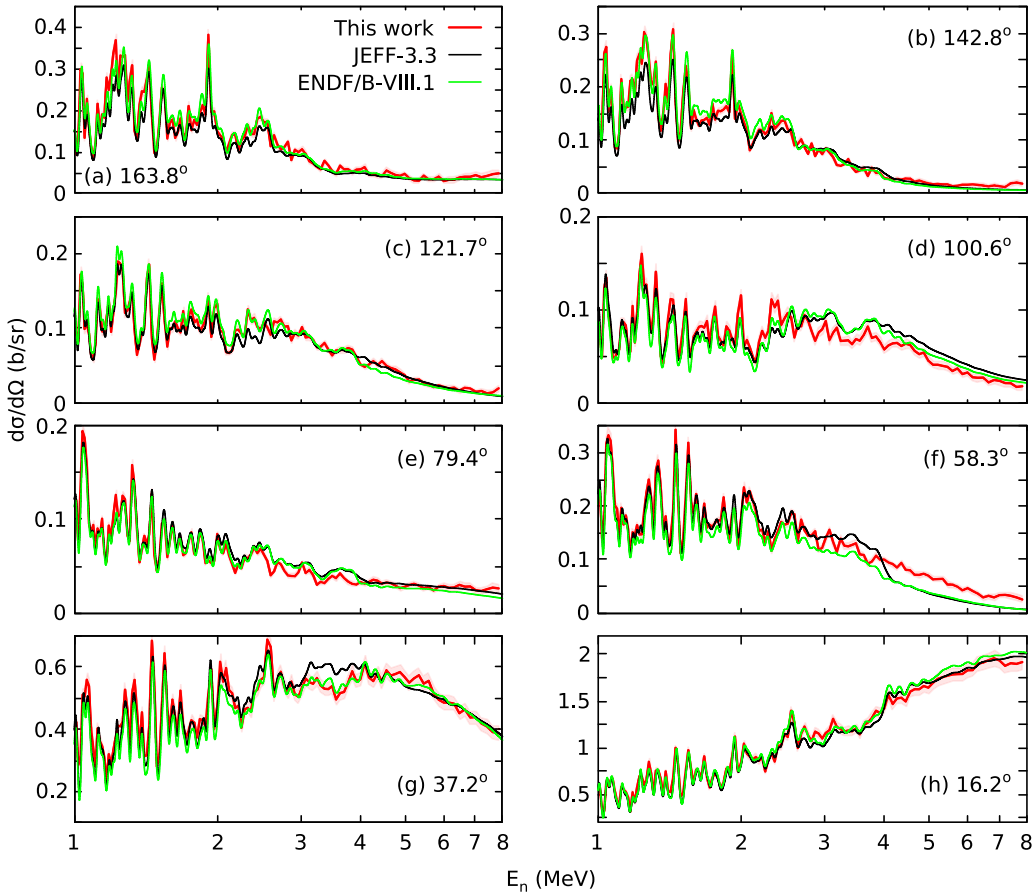

FIG. 8. Differential cross sections of neutron elastic scattering on ^{56}Fe as a function of the neutron incident energy at eight detection angles. The experimental cross sections are compared with the evaluated values provided by JEFF-3.3 [77] and ENDF/B-VIII.1 [16] folded with the experimental energy resolution. The experimental total uncertainties are shown with shaded curves.

resolution, the evaluations were folded accordingly. The results are in excellent agreement with both evaluations across the full neutron energy range, with a total uncertainty varying between 3% and 8%, primarily due to statistical limitations. This agreement confirms the reliability of the response function models developed in this work, as well as the overall analysis procedure, supporting its validity for application to the ^{56}Fe data analysis.

V. ELASTIC SCATTERING CROSS SECTION

The differential cross sections of neutron elastic scattering on ^{56}Fe are presented in Fig. 8 with respect to the incident neutron energy for the eight different detection angles, in the energy range 1–8 MeV. The results are compared with the JEFF-3.3 and ENDF/B-VIII.1 evaluations folded with the experimental energy resolution. In the case of the ^{56}Fe evaluations, ENDF/B-VIII.1 is strongly based on $^{\text{nat}}$Fe high-resolution measurements. Specifically, in the energy range from 1 to 2.2 MeV the angular distributions correspond to refitted Kinney *et al.* [79] $^{\text{nat}}$Fe data. In the energy range from 2.2 to 4 MeV the angular distributions were taken from Smith *et al.* [80] and above 4 MeV neutron incident energy the distributions are based on calculations performed with the EMPIRE [81] code. The JEFF-3.3 angular distributions were adopted by the JEFF-3.0 version which originates from the EFF-2.4 evaluation, updated by Pronyaev *et al.* [82]. The same approach as the one in ENDF/B-VIII.1 was followed, i.e., the high-resolution data from ORELA by Kinney *et al.* [79] were used up to 2.5 MeV. These data are given in 1-keV steps, were converted into relative Legendre coefficients, and the resulting coefficients α_1–α_4 were used to create the file that correctly describes the fine structure of the elastic scattering angular distribution in the unresolved resonance range. In the energy region 2.5–4 MeV the data from ANL by Smith *et al.* [80] were used, and for energies above 4 MeV the evaluation is based on theoretical calculations. There is a relatively good agreement between experimental and evaluated values over the whole neutron energy range. Especially in the 1–3-MeV energy region, where the angular distributions are fluctuating a lot, the agreement between experiment and evaluations, both in cross-section behavior and/or trend and magnitude, is very good within the uncertainties. In the case of the 58.3° detection angle above 4 MeV, the experimental cross section is systematically higher than the values proposed by the evaluations. Similar behavior of the cross section in this detection angle has been observed in previous measurements on iron, $^{\text{nat}}$Fe in Ref. [50] and ^{54}Fe in Ref. [59], making this the third measurement of iron where discrepancies have been observed in this detection angle, suggesting possible issues in the

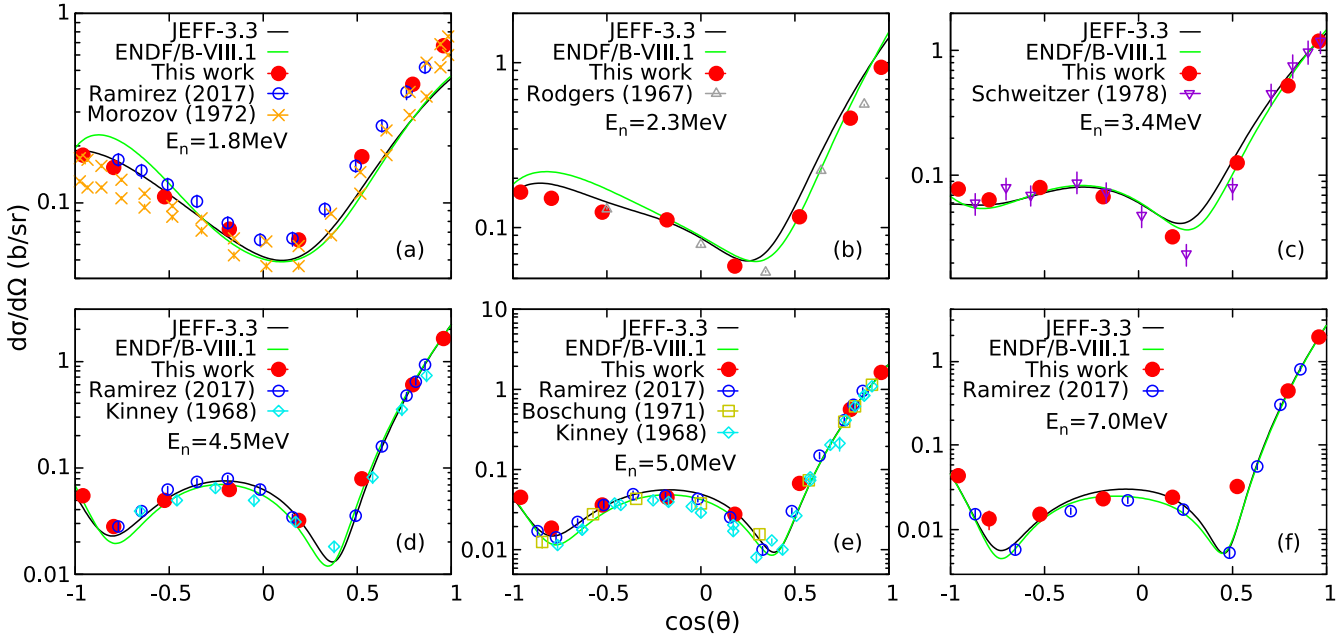

FIG. 9. Comparison of differential cross sections of neutron elastic scattering on ^{56}Fe as a function of the cosine of the scattering angle θ, with data available in the EXFOR [17] library and the angular distributions provided in the JEFF-3.3 [77] and ENDF/B-VIII.1 [16] evaluations. Six 10-ns TOF intervals have been selected. The corresponding incident neutron energy is reported in each graph.

evaluated angular distributions of iron. The total uncertainties of the differential cross sections vary from 3% to 20%, and are mainly generated from the duration of the experiments and their related statistics.

In Fig. 9, the differential cross section is presented as a function of $\cos\theta$ and compared with data from the EXFOR library, as well as angular distributions from the JEFF-3.3 and ENDF/B-VIII.1 evaluations. Six 10-ns time-of-flight intervals were selected to cover most of the neutron energies reported in EXFOR (Table I) within the 1–8-MeV range. Overall, the results of this study show good agreement with previously published experimental data, particularly aligning with the recent measurements by Ramirez *et al.* [25] using quasi-monoenergetic neutron beams. For neutron energies below 3 MeV [see Figs. 9(a) and 9(b)], although the evaluations follow a similar trend, discrepancies in cross-section magnitudes are observed. At higher energies, JEFF-3.3 appears to better reproduce the experimental results compared to ENDF/B-VIII.1, showing consistency with both this work and most of the EXFOR data.

Upon extracting the differential cross sections for elastic scattering, the corresponding Legendre coefficients were also calculated. To achieve this, the cross sections were transformed from the laboratory frame to the center-of-mass frame, and fitted using the following Legendre polynomial expansion:

$$\frac{d\sigma}{d\Omega}(E_n,\theta) = \sum_{l=0} \alpha_l(E_n) P_l(\cos\theta), \tag{7}$$

where $\frac{d\sigma}{d\Omega}$ represents the differential cross section in the center-of-mass frame, α_l are the Legendre polynomial coefficients treated as free parameters in the fit, and P_l are the corresponding Legendre polynomials. The maximum value of l was determined by requiring that the χ^2/ NDF (number of degrees of freedom) of the fit did not decrease upon increasing the order from l to $l+1$. The complete set of extracted Legendre coefficients is provided in Appendix. The results of this fitting process are shown in Fig. 10, for four selected incident neutron energies. From the fitted coefficients, the mean anisotropy $\overline{\mu}$ was also calculated to characterize the angular distribution. This quantity provides a compact and meaningful representation of the scattering angle distribution, indicating the average cosine of the scattering angle in the center-of-mass frame. It is especially relevant in neutron transport calculations, where $\overline{\mu}$ influences the balance between forward and backward scattering. In the evaluated nuclear data file, the angular distributions in the center-of-mass frame are reconstructed using the following expression:

$$f(\mu, E_n) = \sum_{l=0}^{l=n} \frac{2l+1}{2} \beta_l(E_n) P_l(\mu), \tag{8}$$

in which β_l are the normalized Legendre coefficients with $\beta_0 = 1.0$. Based on Eq. (8), the mean anisotropy is given by

$$\overline{\mu} = \int_{-1}^{1} f(\mu, E_n)\mu \, d\mu = \beta_1(E_n). \tag{9}$$

The calculated experimental mean anisotropy is presented in Fig. 11 along with the mean anisotropies from the JEFF-3.3 and ENDF/B-VIII.1 evaluations folded with the experimental energy resolution. It is observed that at low energies, below 2 MeV, the experimental anisotropy of this work is in very good agreement with JEFF-3.3, while ENDF/B-VIII.0 suggests lower values. However, as the energy increases, the mean anisotropy of ENDF/B-VIII.0 seems to more closely

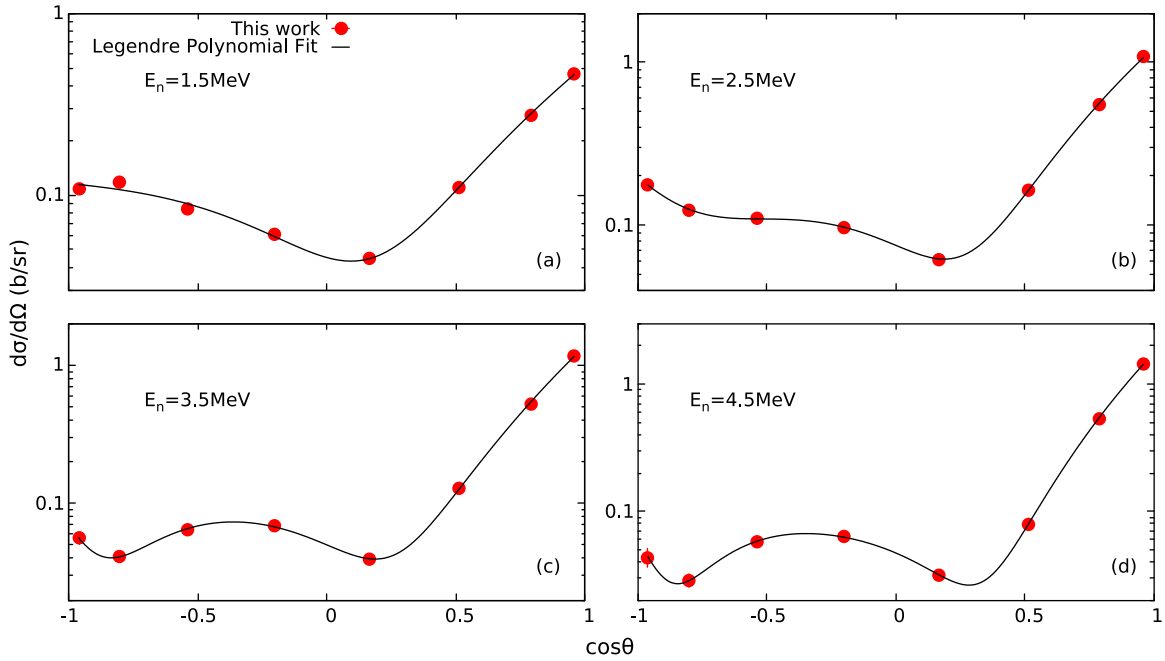

FIG. 10. Angular distributions of neutron elastic scattering on ^{56}Fe for 1.5-, 2.5-, 3.5-, and 4.5-MeV incident neutron energies along with their corresponding Legendre polynomial fits.

follow the experimental trend. From 4 MeV and above, the JEFF-3.3 evaluation shows better agreement with the results of this work within the uncertainties.

Figure 12 presents the angle-integrated neutron elastic scattering cross section, comparing the results with data from the EXFOR library and the JEFF-3.3 and ENDF/B-VIII.1 evaluations, both adjusted for the experimental resolution. In these evaluations, the elastic cross section is derived by subtracting all other partial cross sections from the total. To ensure consistency, the ENDF/B-VIII.1 evaluation was broadened to a 0.3% resolution, aligning well with Kinney *et al.* [19] in the 4–8-MeV range. Above the resonance region, up to 10 MeV, both evaluations adopt the JEFF-3.2 total cross section, based on the Vonach-Tagesen model with fluctuation corrections from Berthold *et al.* [83], including adjustments for minor isotopes. Despite following the same approach for deriving the total cross section, discrepancies between JEFF-3.3 and ENDF/B-VIII.1 appear in their elastic cross sections due to differences in the estimation and subtraction of the nonelastic contributions. The results of this study align well, within uncertainties, with previous experimental data available in EXFOR, especially with the recent measurements by Ramirez *et al.* [25]. In the 1–3-MeV fluctuating region, the present results follow a similar trend to the evaluations,

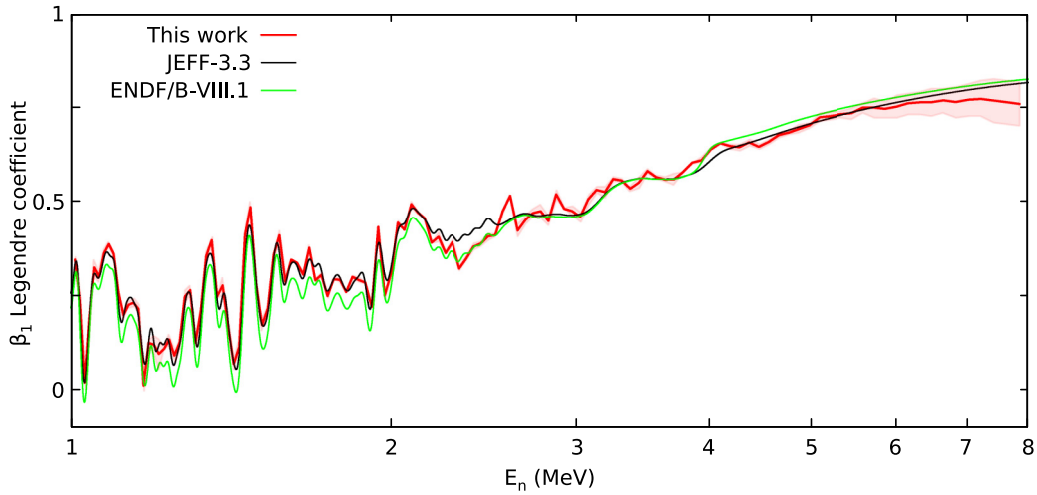

FIG. 11. Comparison of the experimental mean anisotropy $\overline{\mu}$ as a function of neutron incident energy with the corresponding values from the JEFF-3.3 [77] and ENDF/B-VIII.1 [16] evaluated nuclear data libraries. The evaluated distributions have been folded with the experimental energy resolution to allow for direct comparison.

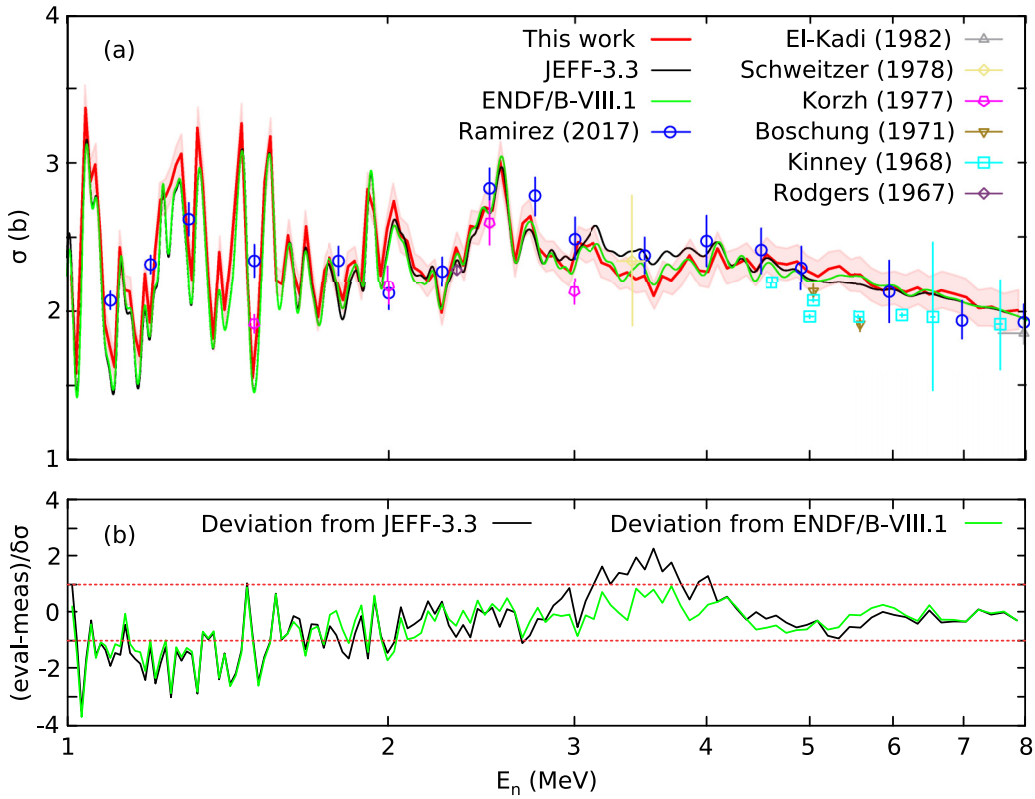

FIG. 12. Angle-integrated cross section of neutron elastic scattering on ^{56}Fe as a function of the incident neutron energy compared with the data available in the EXFOR library [17], and the JEFF-3.3 [77] and ENDF/B-VIII.1 [16] libraries folded with the experimental energy resolution. (b) the deviation of the experimental results from the evaluated values is presented as the difference between evaluation and measurement divided by the experimental uncertainty ($\delta\sigma$).

though they are slightly higher in some cases. From 4 to 8 MeV, where the evaluations diverge, the results of this work lie between them, showing better agreement with ENDF/B-VIII.1 in the 3–4-MeV range and with JEFF-3.3 between 4 and 8 MeV [see Fig. 12(c)]. The total uncertainty of the experimental cross section ranges between 3% and 6%.

VI. INELASTIC SCATTERING CROSS SECTION

The angular distributions of neutron inelastic scattering from the first excited state of ^{56}Fe (0.847 MeV), in the energy range from 2 to 5 MeV, are presented in Fig. 13. The cross sections are given with respect to the neutron incident energy at the eight different detection angles. The results are compared with the JEFF-3.3 and ENDF/B-VIII.1 evaluated libraries folded with the experimental energy resolution. In the evaluated datasets, from the inelastic scattering threshold up to 4 MeV neutron incident energy, fluctuations were imposed in the angular distributions of the first and the second excited states of ^{56}Fe based on the total inelastic scattering cross section data by Dupont *et al.* [84] and Negret *et al.* [47]. Above 4 MeV neutron incident energy the angular distributions of both evaluations are based on statistical model calculations. In most of the detection angles the measured values are slightly higher than the ones provided by the JEFF-3.3 and ENDF/B-VIII.1 evaluations over the whole neutron energy range. In comparison to the evaluations, the better agreement within the experimental uncertainties is observed with ENDF/B-VIII.1. The highest statistical uncertainties occur in the data of the two forward detectors, primarily due to the opposing behavior of the cross sections at these angles. While the elastic scattering cross section increases and becomes the dominant reaction, the inelastic component decreases. For these two detection angles, near the 2-MeV threshold in the present measurement, the cross sections appear to be significantly underestimated compared to the evaluations. Given that the inelastic scattering in these angles corresponds to a small portion of the light output distribution [see Figs. 4(d) and 4(h)] in this energy region, a study was conducted to assess the impact of the response function model parameters on the final results. Based on this analysis, the associated uncertainties were adjusted accordingly. The total uncertainties range from 5% to 35%. Reducing these uncertainties would require significantly longer measurement times.

In Fig. 14 the differential inelastic scattering cross sections are presented as a function of the cosine of the detection angle θ, and compared with the majority of data available in the literature in the overlapping energy region and the JEFF-3.3 and ENDF/B-VIII.1 evaluations. Six 10-ns TOF intervals have been selected, covering a big part of the incident neutron energies that have been measured in other experiments reported in EXFOR (Table II). Based on Fig. 14 issues are observed in the current state of the angular distributions of neutron inelastic scattering on ^{56}Fe. Discrepancies between

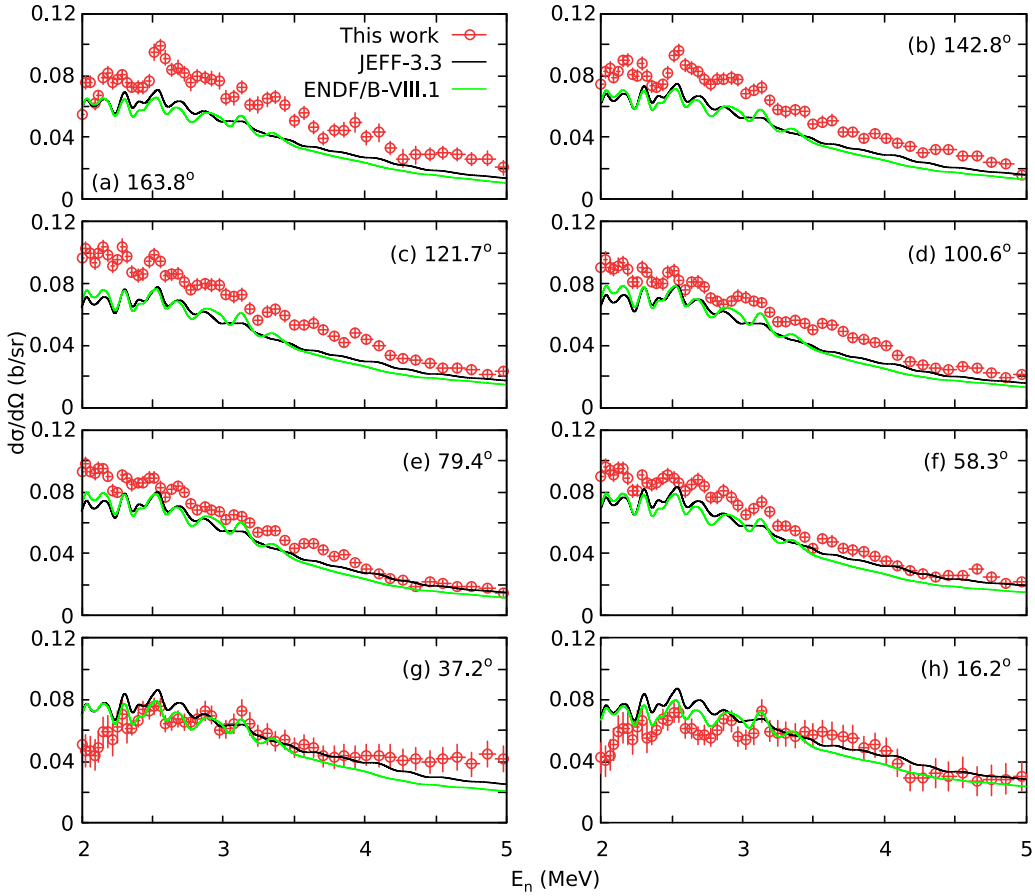

FIG. 13. Differential cross sections of neutron inelastic scattering from the first excited state of ^{56}Fe as a function of the incident neutron energy at the eight detection angles. The experimental cross sections are compared with the evaluated values provided by the JEFF-3.3 [77] and ENDF/B-VIII.1 [16] libraries folded with the experimental energy resolution.

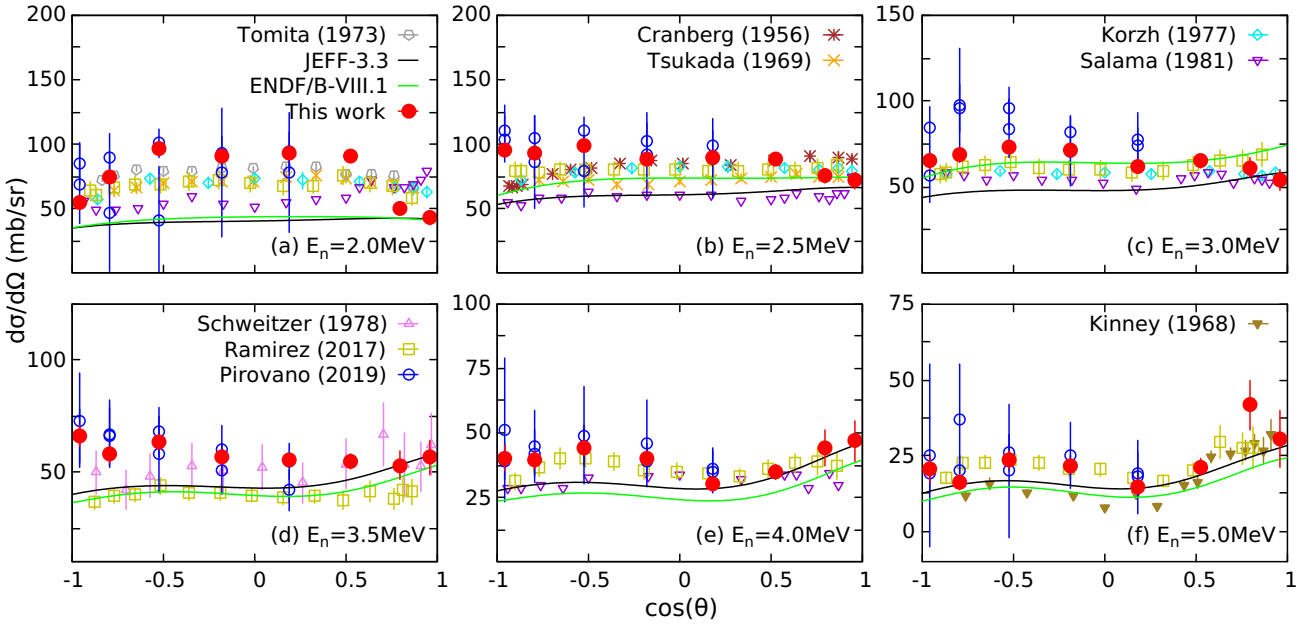

FIG. 14. Comparison of differential cross sections of neutron inelastic scattering from the first excited state of ^{56}Fe as a function of the cosine of the scattering angle θ, with data available in the EXFOR [17] library and the angular distributions provided in the JEFF-3.3 [77] and ENDF/B-VIII.1 [16] evaluations. Six 10-ns TOF intervals have been selected. The corresponding incident neutron energy is reported in each graph. To optimize the visual clarity of the figure, each dataset or evaluation is labeled in only one of the subplots.

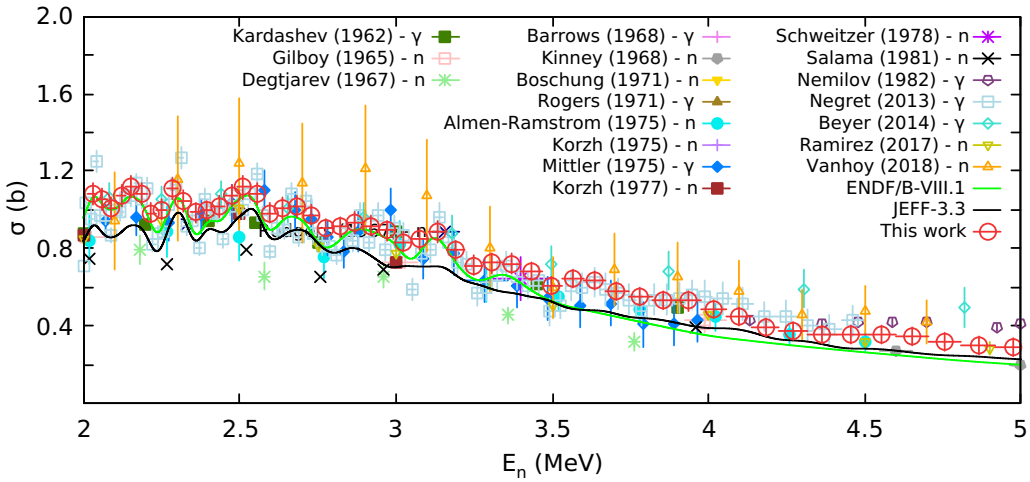

FIG. 15. Angle-integrated cross section of neutron inelastic scattering from the first excited state of ^{56}Fe as a function of the incident neutron energy compared with the data available in the EXFOR library [17], and the JEFF-3.3 [77] and ENDF/B-VIII.1 [16] libraries folded with the experimental energy resolution. Experiments where the γ ray from the deexcitation of the first excited state is detected are labeled with "$-\gamma$", whereas those where the neutron is detected are labeled with "$-n$".

the two evaluations, but also between different experiments, are noted. The results of this work are in agreement in some cases with values reported in other experiments. For the 10-ns TOF intervals that correspond to neutron incident energies below 3 MeV the evaluations clearly deviate from the majority of the experimental cross sections. In the energies above 3 MeV there is a relatively better agreement between evaluations and experiments, including the results of this work, although it is clear that further investigation is needed to assess the quality of both the evaluated and the experimental angular distributions in this energy region.

The results of the angle-integrated neutron inelastic scattering cross section from the first excited state of ^{56}Fe are presented in Fig. 15 in the energy range from 2 to 5 MeV. The results are compared with the data available in the literature, and the JEFF-3.3 and ENDF/B-VIII.1 evaluations folded with the experimental energy resolution. The total uncertainty of the cross section varies between 5% and 16%. There is a good agreement within uncertainties with the ENDF/B-VIII.1 evaluation in the energy range from 2 to 3 MeV. The JEFF-3.3 evaluation seems to support a lower cross section over the whole neutron energy region in contrast with the majority of the experimental data in EXFOR. In comparison with the data available in the literature, there is an overall good agreement within uncertainty with almost all other experiments. It is important to mention that the results of this work are in agreement within uncertainty with the most recent experiments performed by Vanhoy *et al.* [49] and Ramirez *et al.* [25] using quasimononergetic beams at the tandem facility of the University of Kentucky, with the data of Beyer *et al.* [48] from an experiment that was performed at the nELBE facility, but also with another high-resolution measurement performed at GELINA by Negret *et al.* [47] using γ spectrometry by employing the GAINS spectrometer.

In addition to the partial inelastic scattering cross section from the first excited state, an effort was made to extract information from the second excited state as well. Similar to the calculation of the inelastic scattering from the first excited state, the yields that correspond to the inelastic scattering from the second level were extracted by subtracting the contributions of elastic and inelastic scattering from the first level (see Fig. 4), which significantly increased the uncertainties of the resulting cross sections. In the end, partial inelastic scattering cross sections from the second excited state of ^{56}Fe (2.0851 MeV) were produced in the energy range from 3 to 6 MeV, although the uncertainties of these results are considerably high, especially for the angular distributions of the forward angles. The angular distributions in the energy range from 3 to 6 MeV are presented in Fig. 16. The total uncertainties range from 10% to 70%. The cross sections are given with respect to the neutron incident energy at the eight different detection angles. The results are compared with the JEFF-3.3 and ENDF/B-VIII.1 evaluated libraries folded with the experimental energy resolution. In most of the detection angles the results are in agreement with the evaluations within the uncertainties. In some angles (100.6°, 79.4°, 58.3°) above 4-MeV neutron incident energies the results of this work are systematically higher than the evaluations.

In Fig. 17 the differential inelastic scattering cross sections are presented as a function of the cosine of the detection angle θ and compared with the few experimental data available in the literature (see Table III) in the overlapping energy region and the JEFF-3.3 and ENDF/B-VIII.1 evaluations. In the 10-ns interval, that corresponds to 3.25 MeV neutron incident energy [Fig. 17(a)], ENDF/B-VIII.1 seems to follow the data of Tsukada *et al.* [36], while the results of the present work are in better agreement with the JEFF-3.3 evaluation. In the two remaining 10-ns TOF intervals only data by Boschung *et al.* [20] are available for neutron incident energies at 5.05 and 5.58 MeV. In those cases, the results of this work suggest higher cross sections in comparison to the data of Boschung and both the evaluations.

The angle-integrated neutron inelastic scattering cross section from the second level of ^{56}Fe is presented in Fig. 18 in the

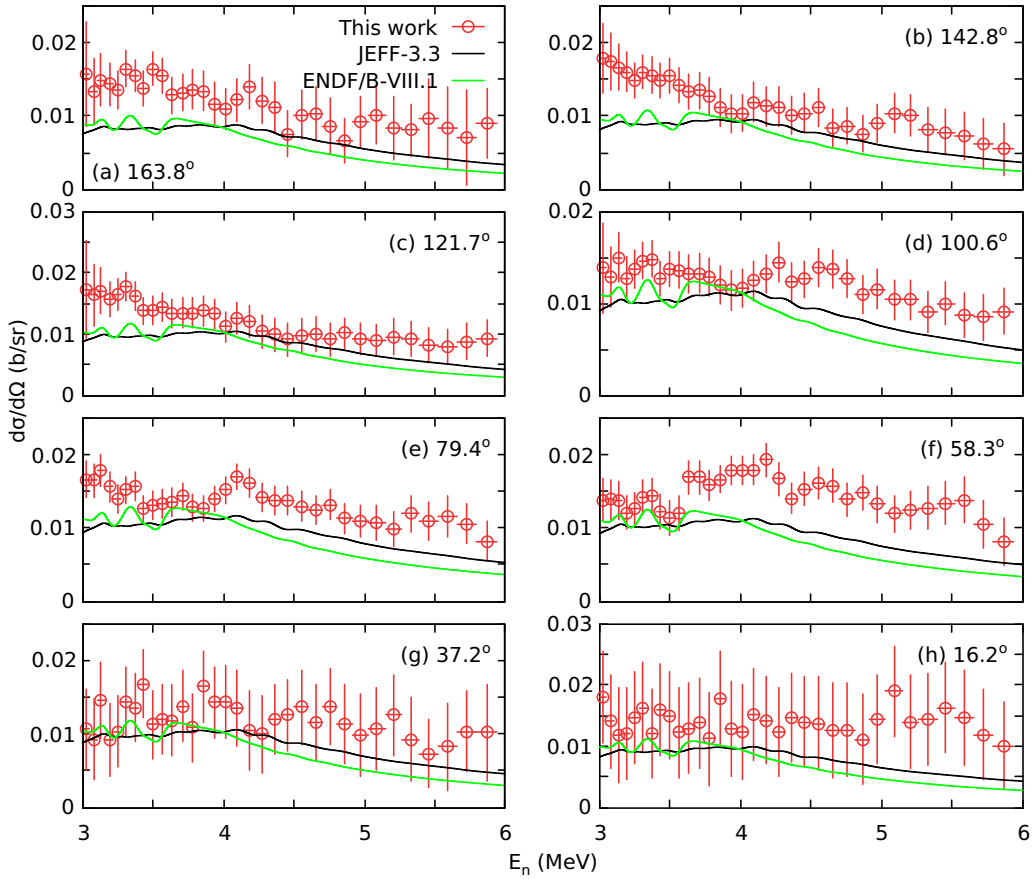

FIG. 16. Differential cross sections of neutron inelastic scattering from the second excited state of ^{56}Fe as a function of the incident neutron energy at the eight detection angles. The experimental cross sections are compared with the evaluated values provided by the JEFF-3.3 [77] and ENDF/B-VIII.1 [16] libraries folded with the experimental energy resolution.

energy range from 3 to 6 MeV. The data are compared with the experimental cross sections available in the EXFOR library, and the JEFF-3.3 and ENDF/B-VIII.1 evaluations folded with the experimental energy resolution. The total uncertainty of the cross section varies between 20% and 45%. An agreement within uncertainties with the ENDF/B-VIII.1 evaluation in the energy range from 3 to 4 MeV is observed, while the JEFF-3.3 evaluation seem to support a lower cross section in this region. Above 4 MeV, JEFF-3.3 supports a higher cross section than ENDF/B-VIII.1, although both evaluations are underestimated in comparison with the results of the present work. In comparison with the data available in EXFOR, there is an overall good agreement within uncertainty with almost all other experiments, even though the present results seem to

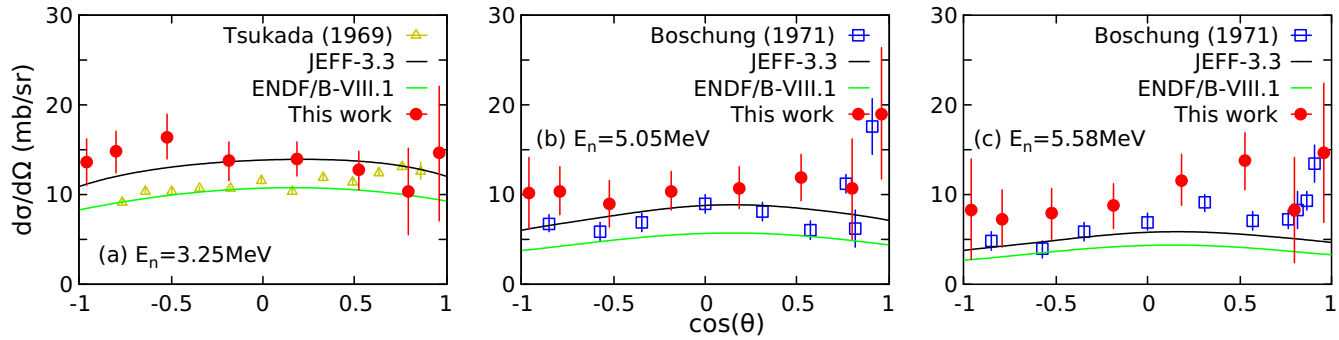

FIG. 17. Comparison of differential cross sections of neutron inelastic scattering from the second excited state of ^{56}Fe as a function of the cosine of the scattering angle θ, with data available in the EXFOR [17] library and the angular distributions provided in the JEFF-3.3 [77] and ENDF/B-VIII.1 [16] evaluations. Three 10-ns TOF intervals have been selected. The corresponding incident neutron energy is reported in each graph.

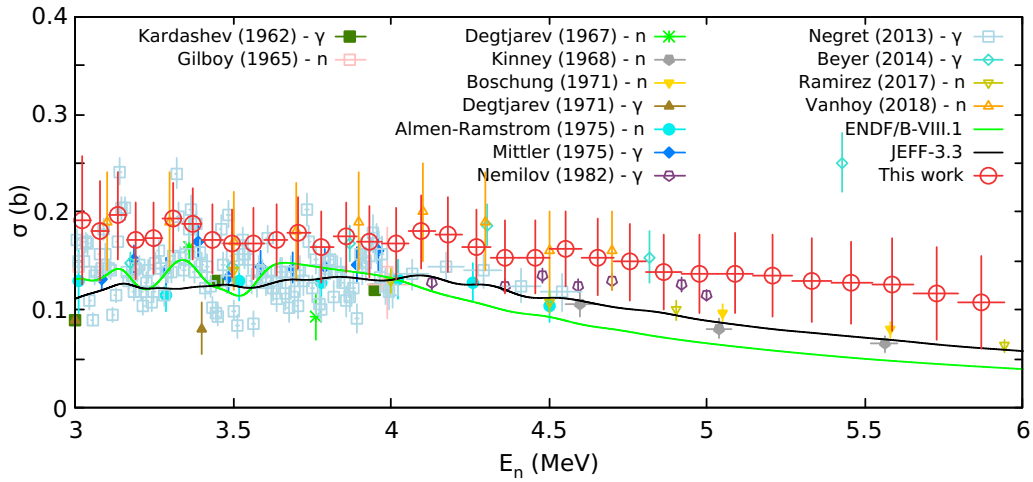

FIG. 18. Angle-integrated cross section of neutron inelastic scattering from the second excited state of ^{56}Fe as a function of the neutron incident energy compared with data available in the EXFOR library [17], and the JEFF-3.3 [77] and ENDF/B-VIII.1 evaluations [16]. Experiments where the γ ray from the deexcitation of the second excited state is detected are labeled with "$-\gamma$", whereas those where the neutron is detected are labeled with "$-n$".

have the highest uncertainties compared to the cross sections from other experiments. Similar to the results from the first excited state, there is a good agreement within uncertainty with the most recent data by Vanhoy *et al.* [49] and Ramirez *et al.* [25], with the data of Beyer *et al.* [48], and also with the high-resolution data of Negret *et al.* [47], although in absolute values the present cross sections are systematically higher.

VII. TOTAL CROSS SECTION

Considering the overlapping energy region between the 1–8-MeV elastic scattering cross section, the 2–5-MeV partial inelastic scattering cross section from the first excited state, and the 3–6-MeV partial inelastic scattering from the second excited state that were extracted from the present experiment, there are some tests that can be made to validate the quality of the results. In the present work, the narrow energy region from 2 to 2.5 MeV was chosen to compare the results with the total cross section of ^{56}Fe. Taking into account the different reaction channels open in this energy region (see Fig. 19), the two dominant reaction mechanisms are the elastic scattering and the inelastic scattering from the first excited state. Other reaction channels are open in this region too, specifically the (n, γ) and (n, n'_2), but their contribution to the total cross section was considered negligible in this test since the cross section of these reactions in this energy region is almost two orders of magnitude lower than the elastic scattering cross section. Nevertheless, the contribution of the (n, γ) reaction, although negligible, was taken from the JEFF-3.3 evaluation and was added with the elastic and inelastic scattering cross sections of the present work. The extracted total cross section of ^{56}Fe in the energy region from 2 to 2.5 MeV is presented in Fig. 20 along with the total cross sections reported in the EXFOR library by Harvey *et al.* [85] and Cornelis *et al.* [86], and the JEFF-3.3 and ENDF/B-VIII.1 evaluations folded with the experimental energy resolution. As mentioned above, both ENDF/B-VIII.1 and JEFF-3.3 evaluations of the total cross section are based on the Berthold *et al.* [83] $^{\text{nat}}$Fe transmission data, corrected for the contribution of the minor isotopes; thus, the resulting cross sections from both evaluations are identical. It is observed that the results of this work are in relatively good agreement within uncertainty with the data of Harvey *et al.* [85] and Cornelis *et al.* [86] above 2.25 MeV neutron incident energy, experiments which were performed with enriched ^{56}Fe samples. The total cross section of this work is underestimated over the whole neutron energy range by the evaluated cross sections, with limited agreement within uncertainties in the energy range above 2.2 MeV.

VIII. THEORETICAL CALCULATIONS

The results of this work are compared with theoretical reaction calculations carried out using the TALYS 1.9 [87,88]

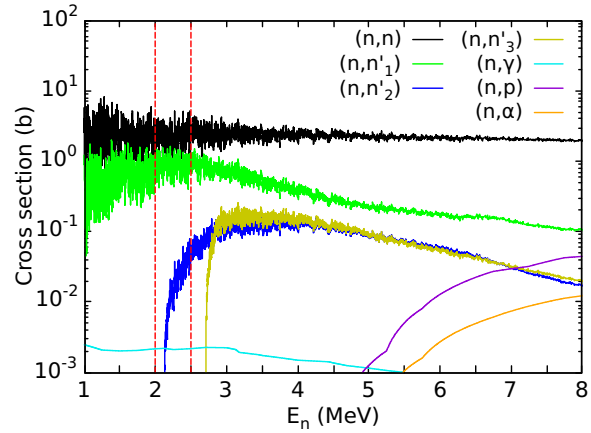

FIG. 19. JEFF-3.3 [77] cross sections of the different reaction channels open in the 1 to 8 MeV energy region for ^{56}Fe. The red lines illustrate the energy region in which the experimental total cross section was calculated.

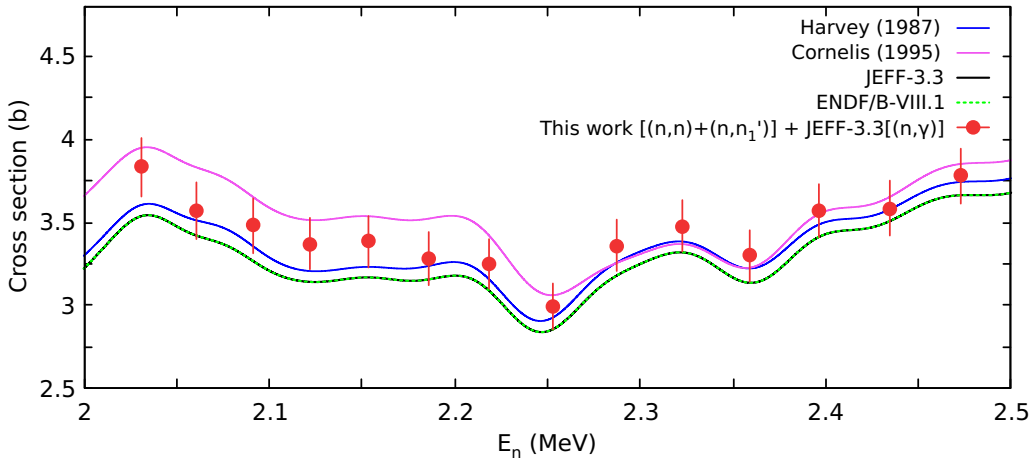

FIG. 20. Total cross section of ^{56}Fe as a function of the incident neutron energy compared with the data available in the EXFOR library [17], and the JEFF-3.3 [77] and ENDF/B-VIII.1 [16] libraries all folded with the experimental energy resolution.

code. The objective of these calculations is to evaluate the predictive limitations of the statistical models, particularly in the neutron energy range covered by the ELISA spectrometer (1–8 MeV), by performing calculations on the one hand using exclusively default parameters and on the other hand using parameters determined from microscopic models. It should be emphasized that in all calculations none of the parameters were fitted on the present data. The calculations covered a neutron incident energy range from 100 keV to 20 MeV.

The "TALYS def." calculation was conducted using the default parameters of the code. The optical model was based on the Koning-Delaroche potential [13], while discrete level information was taken from the Reference Input Parameter Library (RIPL-3) [89]. For levels with unknown spin, parity, or branching ratios, the code assigned values based on statistical rules. The level density was described using the default Constant-Temperature Model (CTM) introduced by Gilbert and Cameron [90], and the γ decay was modeled using the phenomenological γ-strength function by Kopecky and Uhl [91].

In the "TALYS mic.1-2" calculations, the semimicroscopic spherical optical model potential developed by Bauge *et al.* [92] was employed. The level density was described using the latest microscopic approach based on Hartree-Fock-Bogoliubov calculations with the Gogny force [93]. For the γ-ray strength functions, the Gogny-Hartree-Fock-Bogoliubov model was applied, utilizing the D1M version of the Gogny force [94]. The distinction between the two microscopic calculations, "mic.1" and "mic.2", lies in the normalization factor of the optical model's imaginary potential. While "mic.1" uses the default value, "mic.2" incorporates an energy-dependent factor, specifically recommended for neutron energies below 1 MeV.

Figure 21 presents the theoretical calculations for the total, elastic, inelastic, and (n,p) reaction cross sections of ^{56}Fe, compared with the results of this work and existing experimental data. To facilitate comparison, the total cross-section measurements were averaged over 100-keV energy bins. For the ^{56}Fe(n,tot) reaction [Fig. 21(a)], the calculations are compared against the high-resolution measurements of Harvey *et al.* [85] and Cornelis *et al.* [86]. Below 4 MeV neutron energy, only the microscopic calculations show reasonable agreement with experimental values. Above this energy, the "TALYS def." calculation provides a better match to the data, while the microscopic models deviate more significantly in magnitude. Notably, only at neutron energies exceeding 14 MeV does the "TALYS mic.2" calculation converge with the Cornelis *et al.* data.

In Fig. 21(b), the calculated elastic scattering cross sections are compared with the results of this work and data from the EXFOR library. Below 2 MeV, the theoretical models predict higher cross sections than those obtained in this study. Between 2 and 8 MeV, the "TALYS def." calculation agrees with the experimental data within uncertainties, whereas the microscopic models perform poorly in this energy range. Above 8 MeV, "TALYS def." continues to align well with both the trend and magnitude of the sparse experimental data available, while the microscopic calculations appear significantly underestimated. For inelastic scattering cross sections, both total [Fig. 21(c)] and partial [Figs. 21(e) and 21(f)], the theoretical predictions follow the general trend of the experimental data. However, in the total inelastic cross section, the calculations yield higher values than the EXFOR data between 6 and 12 MeV, where the cross section reaches its peak. In the case of partial inelastic scattering from the first excited state of ^{56}Fe, good agreement is observed between the theoretical models, the present results, and literature data over the whole energy region, while for the second excited state the calculations agree well with the data in EXFOR and the results of the present work within uncertainties.

For the (n,p) reaction [Fig. 21(d)], the calculated cross sections are compared with experimental data from the EXFOR library [95–142] and the IRDFF-II evaluation [143], as ^{56}Fe(n,p) is considered a dosimetry standard reaction. The microscopic calculations show good agreement with the experimental data up to 10 MeV but underestimate the cross section by up to 50% at higher energies. Meanwhile, the "TALYS def." calculation follows the overall trend of the

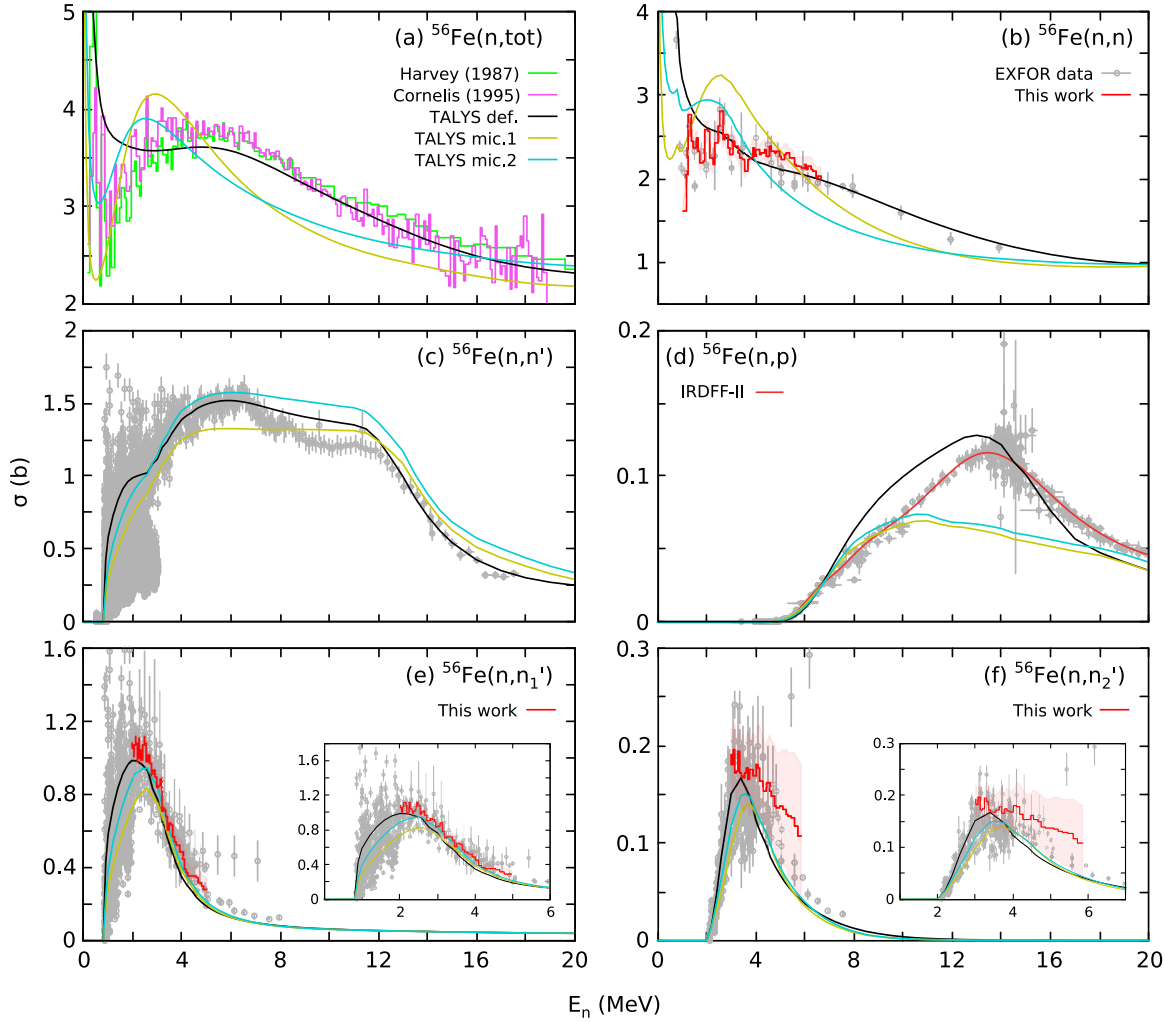

FIG. 21. Comparison between the theoretical calculations of TALYS [87,88] using different sets of parameters and the available experimental data in the literature for the ^{56}Fe total, elastic, inelastic, and (n,p) reaction cross sections. The elastic and inelastic scattering data from this work are also included in the graphs. For the $^{56}\mathrm{Fe}(n,n_1')$ and $^{56}\mathrm{Fe}(n,n_2')$ reaction cross sections, subplots are included focused on the neutron energy regions studied in this work.

IRDFF-II evaluation but overestimates the cross section between 7 and 12 MeV and underestimates it in the 16–20iMeV range.

IX. CONCLUSIONS

A new experiment was conducted at GELINA to measure neutron angular distributions and cross sections for the $^{56}\mathrm{Fe}(n,n)$ and $^{56}\mathrm{Fe}(n,n')$ reactions in the fast neutron energy range. The ELISA spectrometer, consisting of 32 liquid organic scintillators, was used for neutron detection. The analysis procedure included response function modeling for each detector, pulse-shape discrimination, background subtraction, elastic and inelastic separation via kinematic calculations, multiple scattering corrections, and neutron fluence determination. The methodology was validated by successfully reproducing the well-known $^{\mathrm{nat}}\mathrm{C}(n,n)$ reaction cross section. The final results were compared with available EXFOR experimental data and the JEFF-3.3 and ENDF/B-VIII.1 evaluations.

For elastic scattering, this work provides the first high-resolution dataset in the 1–8-MeV range. The Legendre coefficients were extracted to characterize the angular distributions. The uncertainties range from 3% to 20% for the differential cross section and from 3% to 6% for the angle-integrated cross section. The results are in overall agreement with JEFF-3.3, ENDF/B-VIII.1, and previous experimental data above 2 MeV. For inelastic scattering, cross sections were obtained for both the first and second excited states. The first excited state results cover the 2.0–5.0-MeV range, with uncertainties from 3% to 35% for the differential cross section and 6% to 20% for the angle-integrated cross section. The second excited state results range from 3.0 to 6.0 MeV, with uncertainties from 10% to 70% for the differential cross section and 20% to 45% for the angle-integrated cross section. Forward angles exhibit higher uncertainties due to the competing elastic and inelastic cross sections. While the differential

cross sections are slightly higher than ENDF/B-VIII.1, the angle-integrated results align well with JEFF-3.3 and theoretical predictions up to 4 MeV. Additionally, an estimation of the total cross section was extracted in the 2–2.5-MeV range, further validating the results. Finally, the results were compared with theoretical calculations from TALYS 1.9. The "TALYS def." calculation demonstrates good agreement with experimental data, particularly for elastic and total cross sections. Microscopic models ("TALYS mic.1-2") tend to underestimate the cross section in certain energy ranges, emphasizing the need for further refinements in nuclear reaction modeling. This comparison with theoretical predictions using talys highlights the limitations of these models in accurately reproducing neutron scattering cross sections, particularly within the energy range covered by the ELISA spectrometer, reinforcing the importance of precise experimental data.

ACKNOWLEDGMENTS

The authors would like to thank the staff of GELINA for providing the conditions needed for this experiment. This work was partially supported by the Commissariat à l'énergie atomique et aux énergies alternatives (CEA) through the SINET project, and by the European Commission through the projects EUFRAT [144] (EURATOM Contract No. FP7-211499), ARIEL [145] (EURATOM research and training program 2014-2018 under Grant Agreement No. 847594), and APRENDE [146] (HORIZON-EURATOM-2023-NRT-01-06 call under Grant Agreement No. 101164596).

DATA AVAILABILITY

All the data produced from this work will become available via the EXFOR (Experimental Nuclear Reaction Data) library.

APPENDIX: LEGENDRE COEFFICIENTS

The extracted Legendre polynomial coefficients are given in Table VII. The values are in millibarns per steradian for the center-of-mass frame. The corresponding uncertainty of each value originates from the fit of Eq. (7) to the experimental data. The integrated cross section can also be calculated via $4\pi\alpha_0$. The reported incident neutron energy is in the laboratory system.

TABLE VII. Legendre polynomial coefficients in millibarns per steradian for the center-of-mass system. The incident neutron energies are for the laboratory system.

E_n	α_0	α_1	α_2	α_3	α_4	α_5	α_6
1.0099	179 ± 3	185 ± 7	178 ± 8	62 ± 9	−4 ± 10	20 ± 9	
1.0202	120 ± 4	89 ± 8	137 ± 9	27 ± 10			
1.0307	195 ± 5	11 ± 10	150 ± 12				
1.0414	267 ± 6	154 ± 13	226 ± 14				
1.0522	226 ± 9	220 ± 18	169 ± 18				
1.0632	236 ± 6	213 ± 12	253 ± 12				
1.0744	201 ± 4	219 ± 8	266 ± 9	53 ± 9	−28 ± 9		
1.0858	152 ± 2	176 ± 4	186 ± 5	46 ± 4			
1.0973	140 ± 2	151 ± 4	138 ± 5	26 ± 5	−8 ± 5		
1.1090	129 ± 1	100 ± 3	144 ± 3	44 ± 3			
1.1209	193 ± 3	115 ± 7	233 ± 8	72 ± 8			
1.1330	171 ± 3	115 ± 5	193 ± 6	92 ± 6			
1.1453	170 ± 3	117 ± 7	191 ± 8	49 ± 9	28 ± 10	8 ± 11	−15 ± 12
1.1578	147 ± 2	94 ± 5	194 ± 5	44 ± 6			
1.1705	134 ± 3	4 ± 6	179 ± 7				
1.1834	179 ± 3	66 ± 6	206 ± 7	72 ± 8	41 ± 8	13 ± 10	
1.1966	153 ± 6	55 ± 12	188 ± 14				
1.2099	188 ± 12	53 ± 23	224 ± 30				
1.2235	219 ± 2	71 ± 4	270 ± 5	92 ± 5	122 ± 6	15 ± 7	−22 ± 7
1.2373	220 ± 5	87 ± 10	242 ± 12	166 ± 14	65 ± 13		
1.2513	227 ± 5	61 ± 10	264 ± 11	76 ± 13	22 ± 14		
1.2656	237 ± 5	89 ± 11	268 ± 13	66 ± 15	29 ± 16	18 ± 17	
1.2802	243 ± 6	179 ± 14	338 ± 17	70 ± 18	70 ± 18		
1.2949	203 ± 4	161 ± 8	283 ± 10	92 ± 10	14 ± 11		
1.3100	175 ± 3	65 ± 6	223 ± 7	69 ± 8	35 ± 8		
1.3253	256 ± 6	161 ± 12	274 ± 14	65 ± 15	56 ± 16		
1.3408	226 ± 6	240 ± 12	246 ± 14	71 ± 12			
1.3567	177 ± 4	211 ± 8	238 ± 9	59 ± 8			
1.3728	144 ± 1	107 ± 3	225 ± 3	45 ± 3	24 ± 3		
1.3892	190 ± 7	158 ± 16	307 ± 18	98 ± 19	56 ± 19		
1.4059	159 ± 3	80 ± 6	208 ± 7	73 ± 7	79 ± 8		
1.4230	186 ± 4	38 ± 8	227 ± 10	87 ± 11	23 ± 11		
1.4403	224 ± 6	76 ± 12	287 ± 13	95 ± 15			
1.4579	258 ± 9	319 ± 19	356 ± 22	102 ± 22	26 ± 22		
1.4759	178 ± 6	260 ± 13	297 ± 15	139 ± 15	34 ± 14		
1.4942	123 ± 3	103 ± 7	171 ± 8	96 ± 9	21 ± 9		
1.5129	157 ± 4	81 ± 8	201 ± 9	90 ± 10			
1.5319	228 ± 4	147 ± 8	294 ± 10	116 ± 11	21 ± 11		
1.5513	253 ± 5	272 ± 12	379 ± 12	99 ± 11			
1.5710	176 ± 4	216 ± 10	283 ± 11	117 ± 11	22 ± 11		
1.5911	174 ± 3	150 ± 7	233 ± 8	86 ± 9	19 ± 9		
1.6116	200 ± 1	207 ± 1	272 ± 2	105 ± 2	38 ± 2		
1.6325	179 ± 1	181 ± 1	251 ± 1	148 ± 1	45 ± 1	7 ± 1	
1.6538	168 ± 1	154 ± 3	238 ± 4	135 ± 4	52 ± 4	6 ± 5	−14 ± 5
1.6756	205 ± 2	232 ± 5	318 ± 5	156 ± 6	74 ± 6		
1.6977	175 ± 1	152 ± 3	242 ± 3	144 ± 3	29 ± 3	−5 ± 3	
1.7203	156 ± 1	142 ± 3	211 ± 3	93 ± 4	13 ± 4		
1.7434	181 ± 1	135 ± 2	253 ± 3	114 ± 3	54 ± 3	6 ± 4	
1.7669	188 ± 1	165 ± 1	239 ± 1	150 ± 1	53 ± 1	1 ± 1	−1 ± 1
1.7909	175 ± 2	153 ± 4	256 ± 5	113 ± 5	27 ± 5		
1.8154	165 ± 1	128 ± 1	219 ± 1	84 ± 2	4 ± 2	3 ± 2	−3 ± 2
1.8405	183 ± 1	165 ± 2	246 ± 3	60 ± 3	11 ± 3		
1.8660	186 ± 2	163 ± 4	283 ± 5	131 ± 6	79 ± 6	13 ± 7	−8 ± 7
1.8921	171 ± 1	146 ± 2	272 ± 2	146 ± 2	62 ± 2		
1.9187	225 ± 1	148 ± 2	407 ± 2	125 ± 2	78 ± 2	3 ± 2	
1.9459	213 ± 2	276 ± 5	406 ± 6	215 ± 6	106 ± 6	11 ± 5	
1.9736	178 ± 2	133 ± 4	273 ± 5	167 ± 6	72 ± 5		
2.0020	203 ± 2	189 ± 5	269 ± 6	184 ± 7	62 ± 6		
2.0310	219 ± 2	291 ± 5	372 ± 6	191 ± 6	50 ± 6	8 ± 6	−8 ± 6
2.0606	200 ± 1	255 ± 2	327 ± 2	180 ± 2	51 ± 2		
2.0909	196 ± 3	289 ± 7	314 ± 8	165 ± 8	53 ± 7		
2.1218	183 ± 1	258 ± 3	310 ± 4	149 ± 4	49 ± 3		

TABLE VII. (*Continued*.)

E_n	α_0	α_1	α_2	α_3	α_4	α_5	α_6
2.1534	180 ± 1	247 ± 2	327 ± 3	158 ± 3	60 ± 3	6 ± 2	
2.1858	175 ± 1	205 ± 3	306 ± 3	183 ± 3	63 ± 3		
2.2189	180 ± 4	219 ± 9	300 ± 11	207 ± 12	68 ± 11	18 ± 10	
2.2527	158 ± 1	172 ± 2	259 ± 2	164 ± 2	64 ± 2	4 ± 2	
2.2874	179 ± 3	210 ± 7	297 ± 8	186 ± 9	85 ± 8	12 ± 8	
2.3228	193 ± 2	186 ± 5	315 ± 7	239 ± 7	113 ± 7	9 ± 9	−14 ± 9
2.3590	183 ± 2	192 ± 3	282 ± 4	204 ± 4	91 ± 4		
2.3962	205 ± 3	233 ± 7	329 ± 9	245 ± 9	117 ± 8	13 ± 8	
2.4342	204 ± 2	238 ± 5	352 ± 6	211 ± 7	107 ± 6	10 ± 6	
2.4731	215 ± 3	263 ± 7	385 ± 9	246 ± 9	143 ± 8	23 ± 7	
2.5129	214 ± 2	263 ± 4	372 ± 5	251 ± 5	126 ± 4		
2.5538	241 ± 3	342 ± 6	461 ± 7	314 ± 7	159 ± 6		
2.5956	217 ± 2	336 ± 4	425 ± 5	294 ± 4	116 ± 3		
2.6385	186 ± 6	237 ± 14	335 ± 17	251 ± 17	116 ± 15		
2.6824	207 ± 5	280 ± 12	362 ± 13	258 ± 14	98 ± 12		
2.7275	211 ± 5	297 ± 12	378 ± 14	305 ± 14	131 ± 11		
2.7737	195 ± 7	277 ± 17	357 ± 20	284 ± 20	131 ± 17		
2.8211	189 ± 5	255 ± 12	350 ± 13	255 ± 14	106 ± 12		
2.8697	189 ± 5	294 ± 13	360 ± 15	270 ± 14	106 ± 12		
2.9195	184 ± 1	265 ± 2	364 ± 2	298 ± 2	155 ± 2	39 ± 2	27 ± 2
2.9707	181 ± 5	257 ± 12	333 ± 14	268 ± 12	128 ± 11		
3.0233	196 ± 6	271 ± 13	347 ± 16	277 ± 16	127 ± 13		
3.0773	195 ± 6	296 ± 14	369 ± 16	271 ± 16	112 ± 13		
3.1327	196 ± 4	312 ± 9	395 ± 11	337 ± 12	177 ± 11	58 ± 11	34 ± 10
3.1896	185 ± 7	292 ± 16	355 ± 19	310 ± 19	151 ± 14		
3.2481	184 ± 4	309 ± 10	370 ± 11	295 ± 11	124 ± 9		
3.3083	178 ± 2	298 ± 4	365 ± 5	306 ± 5	143 ± 5	31 ± 5	16 ± 4
3.3701	180 ± 3	289 ± 6	372 ± 8	304 ± 9	148 ± 8	33 ± 8	22 ± 7
3.4337	176 ± 7	290 ± 17	346 ± 20	277 ± 19	126 ± 15		
3.4991	179 ± 4	311 ± 9	364 ± 11	306 ± 12	158 ± 11	31 ± 11	18 ± 9
3.5664	167 ± 1	283 ± 3	341 ± 4	304 ± 5	157 ± 4	44 ± 4	24 ± 4
3.6356	178 ± 2	299 ± 5	370 ± 7	326 ± 7	188 ± 7	53 ± 7	29 ± 6
3.7069	175 ± 8	294 ± 17	349 ± 21	326 ± 21	176 ± 16		
3.7803	181 ± 1	315 ± 1	399 ± 1	362 ± 1	203 ± 1	61 ± 1	29 ± 1
3.8560	189 ± 1	343 ± 3	420 ± 4	380 ± 4	208 ± 3	55 ± 3	30 ± 3
3.9339	181 ± 3	331 ± 7	412 ± 9	366 ± 9	212 ± 9	60 ± 9	29 ± 7
4.0142	180 ± 2	346 ± 5	424 ± 7	371 ± 7	231 ± 7	73 ± 6	38 ± 5
4.0970	193 ± 2	380 ± 5	470 ± 7	415 ± 7	266 ± 6	78 ± 6	35 ± 5
4.1824	183 ± 3	355 ± 8	430 ± 11	393 ± 11	243 ± 10	75 ± 10	32 ± 8
4.2705	184 ± 4	356 ± 10	439 ± 14	411 ± 14	262 ± 13	95 ± 13	44 ± 10
4.3614	187 ± 4	369 ± 9	448 ± 12	408 ± 13	255 ± 11	88 ± 11	37 ± 9
4.4553	181 ± 3	351 ± 9	434 ± 12	408 ± 12	254 ± 11	89 ± 11	39 ± 9
4.5522	190 ± 3	375 ± 7	470 ± 10	431 ± 10	283 ± 9	97 ± 9	40 ± 7
4.6523	185 ± 3	376 ± 7	471 ± 9	440 ± 9	297 ± 8	114 ± 8	52 ± 6
4.7558	184 ± 3	378 ± 7	475 ± 10	440 ± 10	291 ± 9	114 ± 8	46 ± 6
4.8628	186 ± 6	386 ± 15	480 ± 20	442 ± 20	290 ± 18	105 ± 17	40 ± 13
4.9735	181 ± 3	381 ± 9	479 ± 12	438 ± 12	299 ± 10	121 ± 10	52 ± 8
5.0879	178 ± 7	386 ± 18	481 ± 24	443 ± 24	311 ± 22	134 ± 19	48 ± 14
5.2064	182 ± 6	396 ± 17	493 ± 22	459 ± 22	319 ± 20	144 ± 18	51 ± 13
5.3291	183 ± 6	401 ± 15	500 ± 20	465 ± 20	321 ± 18	145 ± 16	53 ± 12
5.4562	178 ± 9	392 ± 22	499 ± 30	462 ± 30	333 ± 27	146 ± 24	55 ± 18
5.5879	178 ± 7	399 ± 17	504 ± 23	469 ± 24	337 ± 21	156 ± 19	59 ± 14
5.7245	171 ± 14	384 ± 36	487 ± 49	453 ± 50	326 ± 44	145 ± 40	51 ± 31
5.8661	169 ± 12	377 ± 30	488 ± 41	457 ± 41	343 ± 36	169 ± 33	68 ± 25
6.0131	168 ± 17	379 ± 43	482 ± 58	453 ± 59	334 ± 52	167 ± 47	61 ± 35
6.1656	167 ± 15	381 ± 38	491 ± 52	459 ± 53	344 ± 47	176 ± 43	65 ± 32
6.3241	168 ± 16	384 ± 43	498 ± 58	472 ± 59	357 ± 52	187 ± 47	72 ± 35
6.4888	163 ± 19	374 ± 50	488 ± 67	464 ± 68	367 ± 63	193 ± 55	75 ± 40
6.6601	166 ± 17	382 ± 44	502 ± 59	476 ± 61	373 ± 54	202 ± 47	89 ± 35
6.8382	163 ± 22	373 ± 56	492 ± 76	468 ± 78	371 ± 71	201 ± 62	86 ± 46
7.0236	160 ± 23	369 ± 60	486 ± 82	453 ± 83	356 ± 75	185 ± 66	78 ± 49
7.2167	154 ± 22	356 ± 58	468 ± 80	439 ± 82	346 ± 76	187 ± 68	83 ± 50
7.4179	154 ± 25	355 ± 66	472 ± 90	438 ± 92	352 ± 88	192 ± 78	78 ± 59
7.6276	152 ± 25	348 ± 64	468 ± 87	436 ± 90	359 ± 87	205 ± 76	88 ± 58
7.8465	153 ± 24	348 ± 61	474 ± 83	450 ± 87	369 ± 83	214 ± 73	101 ± 57

[1] D. S. Gelles, Research and development of iron-based alloys for nuclear technology, ISIJ International **30**, 905 (1990).

[2] K. Terrani, S. Zinkle, and L. Snead, Advanced oxidation-resistant iron-based alloys for LWR fuel cladding, J. Nucl. Mater. **448**, 420 (2014).

[3] R. Rebak, Iron-chrome-aluminum alloy cladding for increasing safety in nuclear power plants, EPJ Nucl. Sci. Technol. **3**, 34 (2017).

[4] H. Mori, Y. Oku, Y. Mannami, and T. Kunisada, Iron (III) Oxide-based ceramic material for radiation shielding, Ceramics **3**, 258 (2020).

[5] J. K. Böhlke, J. R. de Laeter, P. De Bièvre, H. Hidaka, H. S. Peiser, K. J. R. Rosman, and P. D. P. Taylor, Isotopic compositions of the elements, 2001, J. Phys. Chem. Ref. Data **34**, 57 (2005).

[6] G. Palmiotti and M. Salvatores, Impact of nuclear data uncertainties on innovative fast reactors and required target accuracies, J. Nucl. Sci. Technol. **48**, 612 (2011).

[7] G. Aliberti, G. Palmiotti, M. Salvatores, T. K. Kim, T. Taiwo, M. Anitescu, I. Kodeli, E. Sartori, J. C. Bosq, and J. Tommasi, Nuclear data sensitivity, uncertainty and target accuracy assessment for future nuclear systems, Ann. Nucl. Energy **33**, 700 (2006).

[8] A. Rivas, N. P. Martin, S. E. Bays, G. Palmiotti, Z. Xu, and J. Hou, Nuclear data uncertainty propagation applied to the versatile test reactor conceptual design, Nucl. Eng. Des. **392**, 111744 (2022).

[9] C. Parisi, C. B. Davis, and G. J. Youinou, Transient analyses of the versatile test reactor using RELAP5-3D, INL/CON-19-53222-Revision-0, Idaho National Laboratory (2019), https://www.osti.gov/biblio/1634108.

[10] M. B. Chadwick, E. Dupont, E. Bauge, A. Blokhin, O. Bouland, D. A. Brown, R. Capote, A. Carlson, Y. Danon, C. De Saint Jean, M. Dunn, U. Fischer, R. A. Forrest, S. C. Frankle, T. Fukahori, Z. Ge, S. M. Grimes, G. M. Hale, M. Herman, A. Ignatyuk, M. Ishikawa, N. Iwamoto, O. Iwamoto, M. Jandel, R. Jacqmin, T. Kawano, S. Kunieda, A. Kahler, B. Kiedrowski, I. Kodeli, A. J. Koning, L. Leal, Y. O. Lee, J. P. Lestone, C. Lubitz, M. MacInnes, D. McNabb, R. McKnight, M. Moxon, S. Mughabghab, G. Noguere, G. Palmiotti, A. Plompen, B. Pritychenko, V. Pronyaev, D. Rochman, P. Romain, D. Roubtsov, P. Schillebeeckx, M. Salvatores, S. Simakov, E. S. Soukhovitskii, J. C. Sublet, P. Talou, I. Thompson, A. Trkov, R. Vogt, and S. Van der Marck, The CIELO Collaboration: Neutron Reactions on ^{1}H, ^{16}O, ^{56}Fe, ^{235,238}U, and ^{239}Pu, Nucl. Data Sheets **118**, 1 (2014).

[11] D. A. Brown, M. B. Chadwick, R. Capote, A. C. Kahler, A. Trkov, M. W. Herman, A. A. Sonzogni, Y. Danon, A. D. Carlson, M. Dunn, D. L. Smith, G. M. Hale, G. Arbanas, R. Arcilla, C. R. Bates, B. Beck, B. Becker, F. Brown, R. J. Casperson, J. Conlin, D. E. Cullen, M. A. Descalle, R. Firestone, T. Gaines, K. H. Guber, A. I. Hawari, J. Holmes, T. D. Johnson, T. Kawano, B. C. Kiedrowski, A. J. Koning, S. Kopecky, L. Leal, J. P. Lestone, C. Lubitz, J. I. Márquez Damián, C. M. Mattoon, E. A. McCutchan, S. Mughabghab, P. Navratil, D. Neudecker, G. P. A. Nobre, G. Noguere, M. Paris, M. T. Pigni, A. J. Plompen, B. Pritychenko, V. G. Pronyaev, D. Roubtsov, D. Rochman, P. Romano, P. Schillebeeckx, S. Simakov, M. Sin, I. Sirakov, B. Sleaford, V. Sobes, E. S. Soukhovitskii, I. Stetcu, P. Talou, I. Thompson, S. van der Marck, L. Welser-Sherrill, D. Wiarda, M. White, J. L. Wormald, R. Q. Wright, M. Zerkle, G. Žerovnik, and Y. Zhu, ENDF/B-VIII.0: The 8th major release of the nuclear reaction data library with CIELO-project cross sections, new standards and thermal scattering data, Nucl. Data Sheets **148**, 1 (2018).

[12] M. Herman, A. Trkov, R. Capote, G. P. A. Nobre, D. A. Brown, R. Arcilla, Y. Danon, A. Plompen, S. F. Mughabghab, Q. Jing, G. Zhigang, L. Tingjin, L. Hanlin, R. Xichao, L. Leal, B. V. Carlson, T. Kawano, M. Sin, S. P. Simakov, and K. Guber, Evaluation of neutron reactions on iron isotopes for CIELO and ENDF/B-VIII.0, Nucl. Data Sheets **148**, 214 (2018).

[13] A. Koning and J. Delaroche, Local and global nucleon optical models from 1 keV to 200 MeV, Nucl. Phys. A **713**, 231 (2003).

[14] M. Diakaki, S. Chen, G. Noguere, D. Bernard, P. Tamagno, and P. Archier, Evaluation of neutron induced reactions on ^{56}Fe with CONRAD, EPJ Web Conf. **239**, 11005 (2020).

[15] International Nuclear Data Evaluation Network (INDEN), https://www-nds.iaea.org/INDEN/.

[16] G. P. A. Nobre, R. Capote, M. T. Pigni *et al.*, ENDF/B-VIII.1: Updated Nuclear reaction data library for science and applications (unpublished).

[17] N. Otuka, E. Dupont, V. Semkova, B. Pritychenko, A. I. Blokhin, M. Aikawa, S. Babykina, M. Bossant, G. Chen, S. Dunaeva, R. A. Forrest, T. Fukahori, N. Furutachi, S. Ganesan, Z. Ge, O. O. Gritzay, M. Herman, S. Hlavač, K. Katō, B. Lalremruata, Y. O. Lee, A. Makinaga, K. Matsumoto, M. Mikhaylyukova, G. Pikulina, V. G. Pronyaev, A. Saxena, O. Schwerer, S. P. Simakov, N. Soppera, R. Suzuki, S. Takács, X. Tao, S. Taova, F. Tárkányi, V. V. Varlamov, J. Wang, S. C. Yang, V. Zerkin, and Y. Zhuang, Towards a more complete and accurate experimental nuclear reaction data library (EXFOR): International Collaboration between nuclear reaction data centres (NRDC), Nucl. Data Sheets **120**, 272 (2014).

[18] W. L. Rodgers, E. F. Shrader, and J. T. Lindow, Neutron scattering from ^{12}C, ^{54}Fe, ^{56}Fe, ^{65}Cu, ^{58}Ni, and ^{60}Ni, Progress Report: Chicago Operations Office, A.E.C., No. 1573-33, 2 (1967).

[19] W. E. Kinney, Neutron elastic and inelastic scattering from ^{56}Fe from 4.60 to 7.55 MeV, Technical Report, ORNL (1968).

[20] P. Boschung, J. T. Lindow, and E. F. Shrader, Scattering of fast neutrons by ^{12}C, ^{54}Fe, ^{56}Fe, ^{58}Ni and ^{60}Ni, Nucl. Phys. A **161**, 593 (1971).

[21] V. M. Morozov, Y. G. Zubov, and N. S. Lebedeva, Two mechanisms of elastic scattering in nuclear optical model, Yaderno-Fizicheskie Issledovaniya v SSSR, No. 14, p. 8 (1972).

[22] I. A. Korzh, V. A. Mishchenko, E. N. Mozhzhukhin, N. M. Pravdivyy, and I. E. Sanzhur, Differential neutron scattering cross-sections at 1.5 to 3.0 MeV for titanium, iron and bismuth nuclei, Ukrainskii Fizichnii Zhurnal **22**, 87 (1977).

[23] T. Schweitzer, D. Seeliger, and S. Unholzer, Elastic and inelastic scattering of 3.4 MeV neutrons by ^{23}Na, ^{24}Mg, ^{27}Al, ^{28}Si, ^{31}P-, ^{55}Mn, ^{56}Fe and ^{209}Bi, Kernenergie **20**, 174 (1977).

[24] S. M. El-Kadi, C. E. Nelson, F. O. Purser, R. L. Walter, A. Beyerle, C. R. Gould, and L. W. Seagondollar, Elastic and inelastic scattering of neutrons from ^{54,56}Fe and ^{63,65}Cu: (I). Measurements from 8 to 14 MeV and a spherical optical model analysis, Nucl. Phys. A **390**, 509 (1982).

[25] A. P. D. Ramirez, J. R. Vanhoy, S. F. Hicks, M. T. McEllistrem, E. E. Peters, S. Mukhopadhyay, T. D. Harrison, T. J. Howard, D. T. Jackson, P. D. Lenzen, T. D. Nguyen, R. L. Pecha, B. G.

Rice, B. K. Thompson, and S. W. Yates, Neutron scattering cross section measurements for ^{56}Fe, Phys. Rev. C **95**, 064605 (2017).
[26] P. H. Stelson and W. M. Preston, The inelastic scattering of fast neutrons from iron, Phys. Rev. **86**, 132 (1952).
[27] J. B. Weddell and B. Jennings, Scattering of 4.4-MeV neutrons by Cr and Mo, and of 6.5-MeV neutrons by Fe (private communication).
[28] L. Cranberg and J. S. Levin, Neutron Scattering at 2.45 Mev by a time-of-flight method, Phys. Rev. **103**, 343 (1956).
[29] D. A. Kardashev, V. S. Stavinskii, D. D. Broder, A. L. Lashuk, and I. P. Sadokhin, Analysis of the excitation functions of the levels of the Fe-56 nucleus in case of inelastic neutron scattering by the optical nuclear model, At. Energ. (USSR) **13** (1962).
[30] D. J. Bredin, Scattering and polarization of neutrons from Al, Si, Fe, and Co at 2 MeV, Phys. Rev. **135**, B412 (1964).
[31] W. Gilboy and J. Towle, A neutron scattering study of Fe^{56}, Nucl. Phys. **64**, 130 (1965).
[32] A. B. Tucker, J. T. Wells, and W. E. Meyerhof, Inelastic neutron scattering near threshold, Phys. Rev. **137**, B1181 (1965).
[33] A. B. Smith, D. Lister, and J. F. Whalen, Microscopic neutron scattering cross-sections for reactor design, Nucl. Data Reactors Conf., Paris **1**, 399 (1966).
[34] J. G. Degtjarev and V. N. Protopopov, Excitation of Al-27, Cr-52, Fe-56 and Bi-209 low levels at inelastic scattering of 1-4 MeV neutrons, At. Energ. **23**, 568 (1967).
[35] A. Barrows, R. Lamb, D. Velkley, and M. McEllistrem, Levels of ^{51}V and ^{55}Mn via $(n, n\gamma)$ reactions, Nucl. Phys. A **107**, 153 (1968).
[36] K. Tsukada, S. Tanaka, Y. Tomita, and M. Maruyama, Elastic and inelastic scattering of fast neutrons from iron, nickel and tungsten, Nucl. Phys. A **125**, 641 (1969).
[37] V. C. Rogers, Spin of the 3120-keV Level in ^{56}Fe, Phys. Rev. C **6**, 801 (1972).
[38] Y. Tomita, Intermediate structure in the neutron scattering cross sections of iron, Nucl. Phys. A **210**, 51 (1973).
[39] S. Elbakr, I. van Heerden, B. Robertson, W. McDonald, G. Neilson, and W. Dawson, The energy level structure of ^{154}Sm from the $(n, n\gamma)$ reaction, Nucl. Phys. A **211**, 493 (1973).
[40] E. S. Konobeevskii, R. M. Musaelyan, V. I. Popov, V. M. Prokopenko, and I. V. Surkova, Inelastic neutron scattering by Ti and Fe isotopes in the energy region near the threshold, Izv. Ross. Akad. Nauk, Ser. Fiz. **37**, 1764 (1973).
[41] I. A. Korzh, V. A. Mishchenko, E. N. Mozhzhukhin, A. A. Golubova, N. M. Pravdivyi, I. E. Sanzhur, and M. V. Pasechnik, Neutron scattering in energy range 1.5-3.0 MeV on the even isotopes of Cr, Ni, Zn, USSR Report to the INDC No. 4, 220 (1975).
[42] E. Ramström, A systematic study of neutron inelastic scattering in the energy range from 2.0 MeV to 4.5 MeV, Aktiebolaget Atomenergi, Stockholm/Studsvik Report No. 503 (1975).
[43] A. Mittler, J. Nardini, and G. P. Couchell, Measurements of neutron inelastic scattering cross sections for natural iron, Nardini thesis, University of Massachusetts at Lowell, MA, USA (1975).
[44] L. S. Lebedev, J. A. Nemilov, A. V. Orlovskij, and L. A. Pobedonostsev, Inelastic scattering of the 4.7 MeV neutrons by Al, Mn, Fe, Ni, Cu and Pb, USSR Report to the INDC No. 3 (1977).
[45] M. Salama, Inelastic scattering of fast neutrons from iron, Atomkernenergie **37**, 221 (1981).
[46] Y. A. Nemilov, L. A. Pobedonostsev, and E. L. Teterin, Inelastic scattering of neutrons on ^{56}Fe nuclei, Atomnaya Energiya **53**, 194 (1982).
[47] A. Negret, C. Borcea, and A. J. M. Plompen, Neutron inelastic scattering measurements for background assessment in neutrinoless double β decay experiments, Phys. Rev. C **88**, 027601 (2013).
[48] R. Beyer, R. Schwengner, R. Hannaske, A. Junghans, R. Massarczyk, M. Anders, D. Bemmerer, A. Ferrari, A. Hartmann, T. Kögler, M. Röder, K. Schmidt, and A. Wagner, Inelastic scattering of fast neutrons from excited states in ^{56}Fe, Nucl. Phys. A **927**, 41 (2014).
[49] J. R. Vanhoy, S. H. Liu, S. F. Hicks, B. M. Combs, B. P. Crider, A. J. French, E. A. Garza, T. Harrison, S. L. Henderson, T. J. Howard, M. T. McEllistrem, S. Nigam, R. L. Pecha, E. E. Peters, F. M. Prados-Estévez, A. P. D. Ramirez, B. G. Rice, T. J. Ross, Z. C. Santonil, L. C. Sidwell, J. L. Steves, B. K. Thompson, and S. W. Yates, ^{54}Fe neutron elastic and inelastic scattering differential cross sections from 2–6 MeV, Nucl. Phys. A **972**, 107 (2018).
[50] E. Pirovano, R. Beyer, M. Dietz, A. R. Junghans, S. E. Müller, R. Nolte, M. Nyman, A. J. M. Plompen, M. Röder, T. Szücs, and M. P. Takacs, Cross section and neutron angular distribution measurements of neutron scattering on natural iron, Phys. Rev. C **99**, 024601 (2019).
[51] OECD nuclear energy agency, nuclear data high-priority request list, https://www.oecd-nea.org/dbdata/hprl/.
[52] W. Mondelaers and P. Schillebeeckx, GELINA, a neutron time-of-flight facility for neutron data measurements, Notiziaro Neutroni e Luce di Sincrotrone **11**, 19 (2006).
[53] D. Ene, C. Borcea, S. Kopecky, W. Mondelaers, A. Negret, and A. Plompen, Global characterisation of the GELINA facility for high-resolution neutron time-of-flight measurements by Monte Carlo simulations, Nucl. Instrum. Methods Phys. Res., Sect. A **618**, 54 (2010).
[54] E. Pirovano, Neutron scattering cross section measurements with a new scintillator array, Ph.D. thesis, Ghent University, 2017.
[55] E. Pirovano, R. Beyer, A. Junghans, R. Nolte, M. Nyman, and A. Plompen, Measurements of neutron scattering angular distributions with a new scintillator setup, EPJ Web Conf. **146**, 11008 (2017).
[56] M. Nyman, T. Adam, C. Borcea, M. Boromiza, P. Dessagne, G. Henning, M. Kerveno, A. Negret, A. Olacel, E. Pirovano *et al.*, New equipment for neutron scattering cross-section measurements at GELINA, EPJ Web Conf. **239**, 17003 (2020).
[57] G. Gkatis, Study of neutron induced reaction cross sections on Fe isotopes at the GELINA facility relevant to reactor applications, Ph.D. thesis, Aix Marseille University and National Technical University of Athens, 2024.
[58] G. Gkatis, E. Pirovano, M. Diakaki, G. Noguere, M. Nyman, A. Oprea, C. Paradela, and A. Plompen, The ELISA spectrometer at the JRC-Geel: Development, achievements and future plans, HNPS Adv. Nucl. Phys. **30**, 11 (2024).
[59] G. Gkatis, M. Diakaki, G. Noguere, M. Nyman, A. Oprea, C. Paradela, E. Pirovano, and A. J. M. Plompen, Cross section measurements of neutron elastic and inelastic scattering on ^{54}Fe, Phys. Rev. C **109**, 034612 (2024).

[60] Eljen Technology, EJ301, EJ309 data sheet, https://eljentechnology.com/products/liquid-scintillators/ej-301-ej-309.

[61] Eljen Technology, EJ315 data sheet, https://eljentechnology.com/products/liquid-scintillators/ej-315.

[62] D. Gedcke and W. McDonald, A constant fraction of pulse height trigger for optimum time resolution, Nucl. Instrum. Methods **55**, 377 (1967).

[63] L. Bardelli, G. Poggi, M. Bini, G. Pasquali, and N. Taccetti, Time measurements by means of digital sampling techniques: A study case of 100 ps FWHM time resolution with a 100 MSample/s, 12 bit digitizer, Nucl. Instrum. Methods Phys. Res., Sect. A **521**, 480 (2004).

[64] M. A. Nelson, B. D. Rooney, D. R. Dinwiddie, and G. S. Brunson, Analysis of digital timing methods with BaF_2 scintillators, Nucl. Instrum. Methods Phys. Res., Sect. A **505**, 324 (2003).

[65] I. A. Pawełczak, S. Ouedraogo, A. Glenn, R. Wurtz, and L. Nakae, Studies of neutron–γ pulse shape discrimination in EJ-309 liquid scintillator using charge integration method, Nucl. Instrum. Methods Phys. Res., Sect. A **711**, 21 (2013).

[66] F. Brooks, A scintillation counter with neutron and gamma-ray discriminators, Nucl. Instrum. Methods **4**, 151 (1959).

[67] J. Polack, M. Flaska, A. Enqvist, C. Sosa, C. Lawrence, and S. Pozzi, An algorithm for charge-integration, pulse-shape discrimination and estimation of neutron/photon misclassification in organic scintillators, Nucl. Instrum. Methods Phys. Res., Sect. A **795**, 253 (2015).

[68] A. Tomanin, J. Paepen, P. Schillebeeckx, R. Wynants, R. Nolte, and A. Lavietes, Characterization of a cubic EJ-309 liquid scintillator detector, Nucl. Instrum. Methods Phys. Res., Sect. A **756**, 45 (2014).

[69] H. Klein and S. Neumann, Neutron and photon spectrometry with liquid scintillation detectors in mixed fields, Nucl. Instrum. Methods Phys. Res., Sect. A **476**, 132 (2002).

[70] N. Kornilov, I. Fabry, S. Oberstedt, and F.-J. Hambsch, Total characterization of neutron detectors with a ^{252}Cf source and a new light output determination, Nucl. Instrum. Methods Phys. Res., Sect. A **599**, 226 (2009).

[71] H. Klein, Neutron spectrometry in mixed fields: NE213/BC501A liquid scintillation spectrometers, Radiat. Prot. Dosim. **107**, 95 (2003).

[72] N. Hawkes, J. Adams, D. Bond, S. Croft, O. Jarvis, and N. Watkins, Measurements of the proton light output function of the organic liquid scintillator NE213 in several detectors, Nucl. Instrum. Methods Phys. Res., Sect. A **476**, 190 (2002).

[73] G. Dietze, Energy calibration of NE-213 scintillation counters by γ-rays, IEEE Trans. Nucl. Sci. **26**, 398 (1979).

[74] C. J. Werner, J. Bull, C. Solomon, F. Brown, G. McKinney, M. Rising, D. Dixon, R. Martz, H. Hughes, L. Cox *et al.*, MCNP6.2 release notes, LANL Report LA-UR-18-20808 (2018).

[75] C. J. Werner *et al.*, MCNP users manual-code version 6.2, LANL Report LA-UR-17-29981 (2017).

[76] A. Carlson, V. Pronyaev, R. Capote, G. Hale, Z.-P. Chen, I. Duran, F.-J. Hambsch, S. Kunieda, W. Mannhart, B. Marcinkevicius, R. Nelson, D. Neudecker, G. Noguere, M. Paris, S. Simakov, P. Schillebeeckx, D. Smith, X. Tao, A. Trkov, A. Wallner, and W. Wang, Evaluation of the neutron data standards, Nucl. Data Sheets **148**, 143 (2018).

[77] A. Plompen, O. Cabellos, C. De Saint Jean, M. Fleming, A. Algora, M. Angelone, P. Archier, E. Bauge, O. Bersillon, A. Blokhin, F. Cantargi, A. Chebboubi, C. J. Diez, H. Duarte, E. Dupont, J. Dyrda, B. Erasmus, L. Fiorito, U. Fischer, D. Flammini, D. Foligno, M. Gilbert, J. R. Granada, W. Haeck, F. Hambsch, P. Helgesson, S. Hilaire, I. Hill, M. Hursin, R. Ichou, R. Jacqmin, B. Jansky, C. Jouanne, M. Kellett, D. H. Kim, H. I. Kim, I. Kodeli, A. J. Koning, A. Y. Konobeyev, S. Kopecky, B. Kos, A. Krasa, L. Leal, N. Leclaire, P. Leconte, Y. O. Lee, H. Leeb, O. Litaize, M. Majerle, J. Marquez Damian, F. Michel-Sendis, R. Mills, B. Morillon, G. Noguere, M. Pecchia, S. Pelloni, P. Pereslavtsev, R. Perry, D. Rochman, R. Roehrmoser, P. Romain, P. Romojaro, D. Roubtsov, P. Sauvan, P. Schillebeeckx, K. Schmidt, O. Serot, S. Simakov, I. Sirakov, H. Sjöstrand, A. Stankovskiy, J. C. Sublet, P. Tamagno, A. Trkov, S. Van Den Marck, F. Velarde, R. Villari, K. Yokoyama, and G. Zerovnik, The Joint Evaluated Fission and Fusion Nuclear Data Library, JEFF-3.3, Eur. Phys. J. A **56**, 181 (2020).

[78] G. Gkatis, E. Pirovano, M. Diakaki, G. Noguere, M. Nyman, A. Oprea, C. Paradela, and A. J. M. Plompen, Angular distribution measurements of neutron elastic scattering on natural carbon, Phys. Rev. C **110**, 034609 (2024).

[79] W. E. Kinney and J. W. McConnell, High resolution neutron scattering experiments at ORELA, *International Conference on Interaction of Neutrons with Nuclei* (Lowell, USA, 1976), Vol. 2, p. 1319.

[80] A. Smith and P. Guenther, Scattering of MeV neutrons from elemental iron, Nucl. Sci. Eng. **73**, 186 (1980).

[81] M. Herman, R. Capote, B. Carlson, P. Obložinský, M. Sin, A. Trkov, H. Wienke, and V. Zerkin, EMPIRE: Nuclear reaction model code system for data evaluation, Nucl. Data Sheets **108**, 2655 (2007).

[82] V. Pronyaev, S. Tagesen, H. Vonach, and S. Badikov, Improvement of the EFF-2 evaluations for ^{52}Cr, ^{56}Fe, ^{58}Ni and ^{60}Ni, Final Report for NET (1995).

[83] K. Berthold, C. Nazareth, G. Rohr, and H. Weigman, High-resolution Fe transmission data from Geel (private communication).

[84] E. Dupont, P. Ribon, H. Weigmann, and G. Vanpraet, High resolution measurement of the neutron inelastic scattering cross section of ^{56}Fe, *Conference on Nuclear Data for Science and Technology* (Trieste, Italy, 1997), p. 529.

[85] J. A. Harvey (private communication).

[86] G. Rohr, R. Shelley, and C. Nazareth, Total neutron cross section measurement of vanadium (private communication).

[87] A. J. Konning, S. Hilaire, and M. C. Duijvestijn, TALYS-1.0, EDP Sciences, Les Ulis, France, 211 (2008).

[88] TALYS 1.9, https://www-nds.iaea.org/talys/ (2025).

[89] R. Capote, M. Herman, P. Obložinský, P. Young, S. Goriely, T. Belgya, A. Ignatyuk, A. Koning, S. Hilaire, V. Plujko, M. Avrigeanu, O. Bersillon, M. Chadwick, T. Fukahori, Z. Ge, Y. Han, S. Kailas, J. Kopecky, V. Maslov, G. Reffo, M. Sin, E. Soukhovitskii, and P. Talou, RIPL – Reference input parameter library for calculation of nuclear reactions and nuclear data evaluations, Nucl. Data Sheets **110**, 3107 (2009), special Issue on Nuclear Reaction Data.

[90] A. Gilbert and A. G. W. Cameron, A composite nuclear-level density formula with shell corrections, Can. J. Phys. **43**, 1446 (1972).

[91] J. Kopecky and M. Uhl, Test of γ-ray strength functions in nuclear reaction model calculations, Phys. Rev. C **41**, 1941 (1990).

[92] E. Bauge, J. P. Delaroche, and M. Girod, Lane-consistent, semimicroscopic nucleon-nucleus optical model, Phys. Rev. C **63**, 024607 (2001).

[93] S. Hilaire, M. Girod, S. Goriely, and A. J. Koning, Temperature-dependent combinatorial level densities with the D1M Gogny force, Phys. Rev. C **86**, 064317 (2012).

[94] S. Goriely, S. Hilaire, S. Péru, and K. Sieja, Gogny-HFB+QRPA dipole strength function and its application to radiative nucleon capture cross section, Phys. Rev. C **98**, 014327 (2018).

[95] M. Kostal, T. Czakoj, P. Alexa, J. Šimon, M. Zmeškal, M. Schulc, A. Krechlerová, T. Peltán, F. Mravec, F. Cvachovec, V. Rypar, R. Uhlář, O. Harkut, and Z. Matěj, Measurement of dosimetrical cross sections with 14.05 MeV neutrons from compact neutron generator, Ann. Nucl. Energy **191**, 109904 (2023).

[96] A. A. Filatenkov, Neutron activation cross sections measured at KRI in neutron energy region 13.4-14.9 MeV, USSR Report to the INDC (2016).

[97] V. K. Mulik, H. Naik, S. V. Suryanarayana, S. D. Dhole, P. M. Prajapati, B. S. Shivashankar, K. C. Jagadeesan, S. V. Thakre, V. N. Bhoraskar, and A. Goswami, Measurement of ^{56}Fe(n, p)^{56}Mn reaction cross-section at $E_n = 5.9$, 9.85, 14.8 and 15.5 MeV, J. Radioanal. Nucl. Chem. **296**, 1321 (2013).

[98] A. Fessler, A. J. M. Plompen, D. L. Smith, J. W. Meadows, and Y. Ikeda, Neutron Activation cross-section measurements from 16 to 20 MeV for isotopes of F, Na, Mg, Al, Si, P, Cl, Ti, V, Mn, Fe, Nb, Sn, and Ba, Nucl. Sci. Eng. **134**, 171 (2000).

[99] Y. Ikeda, C. KONNO, Y. OYAMA, K. KOSAKO, K. OISHI, and H. MAEKAWA, Absolute measurements of activation cross sections of ^{27}Al(n,p)^{27}Mg, Al^{27}(n,A)^{24}Na, ^{56}Fe(n,p)^{56}Mn, ^{90}Zr(n,2n)$^{89m+g}$Zr and ^{93}Nb(n,2n)^{92m}Nb at energy range of 13.3–14.9 MeV, J. Nucl. Sci. Technol. **30**, 870 (1993).

[100] B. Zongyu, R. Chaofan, Y. Xiaoyun, Z. Shuping, D. Shengyao, and Y. Yiguan, Absolute measurement of cross sections of ^{27}Al(n,A)^{24}Na and ^{56}Fe(n,p)^{56}Mn at E_n=14.6 MeV, Chin. J. Nucl. Phys. **15**, 341 (1993).

[101] M. Belgaid, M. Siad, and M. Allab, Measurement of 14.7 MeV neutron cross sections for several isotopes, J. Radioanal. Nucl. Chem. **166**, 493 (1992).

[102] P. Fuga, Study of the excitation function of ^{56}Fe(n,p)^{56}Mn threshold reaction, Nucl. Instrum. Methods Phys. Res., Sect. A **309**, 500 (1991).

[103] J. Meadows, D. Smith, M. Bretscher, and S. Cox, Measurement of 14.7 MeV neutron-activation cross sections for fusion, Ann. Nucl. Energy **14**, 489 (1987).

[104] Z. Muyao, Z. Yongfa, W. Chuanshan, Z. Lu, C. Yitai, Z. Shuxin, Z. Shenjun, X. Kuanzhong, Z. Shenmuo, C. Xueshi, Z. Yiping, and Y. Qinguan, Shell effect from the cross section of the (n,2n) reaction produced by 14.6 MeV neutron, Chin. J. Nucl. Phys. **9**, 34 (1987).

[105] J. P. Gupta, H. D. Bharwaj, and R. Prasad, Pre-equilibrium emission effect in (n,p) reaction cross-sections at 14.8 MeV, Pramana J. Phys. **24**, 637 (1985).

[106] K. Kudo, Cross section measurements of ^{56}-Fe(n,p)^{56}-Mn and ^{27}-Al(n,α)^{24}-Na between 14.0 and 19.9 MeV (private communication).

[107] P. N. Ngoc, L. L. Bach, N. V. Do, T. T. Vinh, and I. Ribansky, Neutron activation cross section for ^{56}Fe(n,p) and ^{87}Rb(n,2n) reactions, Vietnam Report to the INDC No. 2 (Austria, 1983).

[108] K. Kudo, ^{56}Fe(n,p)^{56}Mn Cross Section at 14.60 MeV, Japanese report to NEANDC (1982).

[109] P. N. Ngoc, S. Gueth, F. Deak, and A. Kiss, Investigations of (n,p), (n,a) and (n,2n) reactions around 14 MeV, Ph.D. Thesis, Eotvos Lorand University, 1980.

[110] T. B. Ryves, P. Kolkowski, and K. J. Zieba, Cross section measurements of ^{56}Fe(n, p)^{56}Mn, ^{63}Cu(n, 2n)^{62}Cu and ^{65}Cu(n, 2n)^{64}Cu between 14 and 19 MeV, Metrologia **14**, 127 (1978).

[111] L. Chi-Chou, L. Han-Lin, F. Pei-Kuo, M. Hung-Chang, and L. Yeh-Sha, Cross section measurement for the reaction ^{56}Fe(n,p)^{56}Mn, High Energy Phys. Nucl. Phys. Chin. ed. **2**, 550 (1978).

[112] D. Sharma, M. G. Shahani, U. Y. Phadnis, and S. K. Sadavarte, Absolute measurements of Fe-56(n,p)Mn-56 cross-section at 14.7 MeV using a neutron telescope, *21. Nucl. Phys. and Solid State Phys. Symp., Bombay* (India, 1978), Vol. 2, p. 349.

[113] Y. A. Nemilov and Y. N. Trofimov, Cross-sections of (n,p) reactions in the isotopes ^{58}Ni, ^{56}Fe and ^{64}Zn for neutron energies of 7.6-9.3 MeV, Yad.-Fiz. Issled. SSSR **27**, 25 (1978).

[114] S. L. Sothras, A study of the systematics for (n,2n) reactions, Ph.D. Thesis, Southern Methodist University, 1977.

[115] K. Kudo, Absolute measurement of the ^{56}Fe(n,p)^{56}Mn cross section at 14.8 MeV using an on-line monitoring system for the time variation of neutron flux, Nucl. Instrum. Methods **141**, 325 (1977).

[116] Z. A. Ramendik, G. M. Stukov, and V. T. Shchebolev, Determination of the ^{56}Fe(n,p)^{56}Mn cross section at 14.8 MeV, Atomnaya Energiya **42**, 136 (1977).

[117] A. B. M. G. Mostafa, Measurements of relative neutron activation cross sections of ^{27}Al(n,p)^{27}Mg, ^{27}Al(n,a)^{24}Na, ^{24}Mg(n,p)^{24}Na and ^{56}Fe(n,p)^{56}Mn reactions in the energy range of 4.5 to 8.35 MeV, Nucl. Sci. Appl. B **9**, 10 (1976).

[118] R. Spangler, E. L. Draper, Jr., and T. A. Parish, 14-MeV cross section measurements of threshold reactions for seven metals, Trans. Am. Nucl. Soc. **22** (1975).

[119] J. C. Robertson, B. N. Audric, and P. Kolkowski, The ^{56}Fe(n,p)^{56}Mn and ^{27}Al(n,a)^{24}Na cross sections at $14 \cdot 78$ MeV, J. Nucl. Energy **27**, 139 (1973).

[120] N. C. Dyer and J. H. Hamilton, ^{56}Fe and ^{58}Fe(n,p) cross sections for $14 \cdot 4$ MeV neutrons, J. Inorg. Nucl. Chem. **34**, 1119 (1972).

[121] V. Levkovsky, G. E. Kovelskaya, G. P. Vinitskaya, V. M. Stepanov, and V. V. Sokolsky, Cross Sections of the (n,p) and (n,a) Reactions at 14.8 MeV, Sov. J. Nucl. Phys. **8**, 4 (1969).

[122] H. K. Vonach, W. G. Vonach, H. Muenzer, and P. Schramel, Precision measurements of excitation functions of (n,p),(n,alpha) and (n,2n) reactions induced by 13.5-14.7 MeV neutrons, *Nuclear Cross-Sections Technology Conference* (Washington, USA, 1968), Vol. 2, p. 885.

[123] P. Cuzzocrea, E. Perillo, and S. Notarrigo, Some excitation functions of neutron-induced reactions around 14 MeV, Il Nuovo Cimento B **54**, 53 (1968).

[124] J. A. Grundl, A study of fission-neutron spectra with high-energy activation detectors—Part I. Detector development and excitation measurements, Nucl. Sci. Eng. **30**, 39 (1967).

[125] H. Liskien and A. Paulsen, Cross sections for the Cu^{63}(n,α)Co^{60}, Ni^{60}(n,p)Co^{60} and some other threshold reac-

tions using neutrons from the $Be^{9}(\alpha,n)C^{12}$ reaction, Nukleonik **8**, 315 (1966).

[126] J. D. Hemingway, R. H. James, E. B. M. Martin, and G. R. Martin, The determination of the cross sections for the reactions $^{27}Al(n, a)$ and $^{56}Fe(n, p)$ for 14 MeV neutrons by an absolute method, Proc. R. Soc. A Math. Phys. Eng. Sci. **292** (1966).

[127] H. Liskien and A. Paulsen, Cross-section measurement for the threshold reactions $^{56}Fe\ (n,p)\ ^{56}Mn$, $^{59}Co\ (n,a)\ ^{56}Mn$ and $^{63}Cu\ (n,2n)\ ^{62}Cu$ between $12 \cdot 6$ and $19 \cdot 6$ MeV neutron energy, J. Nucl. Energy, Parts A/B **19**, 73 (1965).

[128] M. Bormann, E. Fretwurst, P. Schehka, G. Wrege, H. Büttner, A. Lindner, and H. Meldner, Some excitation functions of neutron induced reactions in the energy range 12.6–19.6 MeV, Nucl. Phys. **63**, 438 (1965).

[129] D. C. Santry and J. P. Butler, Excitation curves for the reactions $Fe^{56}(n, p)Mn^{56}$ and $Co^{59}(n,a)Mn^{56}$, Can. J. Phys. **42** (1964).

[130] G. Bonazzola, P. Brovetto, E. Chiavassa, R. Spinoglio, and A. Pasquarelli, The measurement by activation of cross sections for 14.7 MeV neutrons, Nucl. Phys. **51**, 337 (1964).

[131] W. G. Cross and H. L. Pai, Activation cross sections in Ti for 14.5 MeV neutrons, *Canadian report to EANDC*, No. 16 (France, 1963), p. 1.

[132] F. Gabbard and B. D. Kern, Cross sections for charged particle reactions induced in medium weight nuclei by neutrons in the energy range 12-18 MeV, Phys. Rev. **128**, 1276 (1962).

[133] M. Bormann, S. Cierjacks, R. Langkau, and H. Neuert, Ìber die Wirkungsquerschnitte einigern n, nα-Reaktionen für Neutronenenergien zwischen 12 und 19 MeV, Z. Phys. **166**, 477 (1962).

[134] D. M. Chittenden, D. G. Gardner, and R. W. Fink, New isotope of manganese; cross sections of the iron isotopes for 14.8-Mev Neutrons, Phys. Rev. **122**, 860 (1961).

[135] M. J. Depraz, G. Legros, and M. R. Salin, Mesure des sections efficaces de quelques réactions (n,p), (n,a), (n,2n), J. Phys. Radium **21**, 377 (1960).

[136] B. D. Kern, W. E. Thompson, and J. M. Ferguson, Cross sections for some (n, p) and (n, a) reactions, Nucl. Phys. **10**, 226 (1959).

[137] J. Terrell and D. M. Holm, Excitation Function for $Fe^{56}(n, p)Mn^{56}$, Phys. Rev. **109**, 2031 (1958).

[138] S. Yasumi, Nuclear reactions induced by the 14 MeV neutrons, J. Phys. Soc. Jpn. **12**, 443 (1957).

[139] D. L. Allan, Protons from the interaction of 14 MeV neutrons with medium weight nuclei, Proc. Phys. Soc. Sect. A **70**, 195 (1957).

[140] G. W. Mcclure and D. W. Kent, Inelastic scattering of 14 MeV neutrons, J. Franklin Inst. **260**, 238 (1955).

[141] E. B. Paul and R. L. Clarke, Cross-section measurements of reactions induced by neutrons of 14.5 MeV energy, Can. J. Phys. **31**, 267 (1953).

[142] S. G. Forbes, Activation cross sections for 14-Mev neutrons, Phys. Rev. **88**, 1309 (1952).

[143] A. Trkov, P. Griffin, S. Simakov, L. Greenwood, K. Zolotarev, R. Capote, D. Aldama, V. Chechev, C. Destouches, A. Kahler, C. Konno, M. Koštál, M. Majerle, E. Malambu, M. Ohta, V. Pronyaev, V. Radulović, S. Sato, M. Schulc, E. Šimečková, I. Vavtar, J. Wagemans, M. White, and H. Yashima, IRDFF-II: A new neutron metrology library, Nucl. Data Sheets **163**, 1 (2020).

[144] S. Oberstedt, G. Sibbens, S. Kopecky, M. Nyman, Y. Aregbe, A. Göök, A. Plompen, C. Paradela, M. Hult, J. Heyse, and P. Schillebeeckx, EUFRAT, Open Access to the nuclear research infrastructure at JRC Geel – Summary report 2017-2018, European Commission, Joint Research Centre (2018), https://data.europa.eu/doi/10.2760/798329.

[145] C. Franzen, A. Junghans, E. M. Gonzalez, and A. J. M. Plompen, ARIEL & SANDA nuclear data activities, EPJ Nucl. Sci. Technol. **8**, 19 (2022).

[146] APRENDE, Addressing PRiorities of Evaluated Nuclear Data in Europe, https://aprende-project.eu/home.